This is the post-print, accepted manuscript in *IEEE Journal of Oceanic Engineering*: "A maneuvering model for an underwater vehicle near a free surface—Part III: Simulation and control under waves," F. Valentinis, T. Battista, and C. A. Woolsey. *IEEE J. Oceanic Engineering*, **48**(3), pp. 752-777, 2023. [DOI: 10.1109/JOE.2023.3234811]

A Maneuvering Model for an Underwater Vehicle Near a Free Surface—Part III : Simulation and Control Under Waves

Francis Valentinis[*], Thomas Battista[†], and Craig Woolsey[‡]

Abstract. This paper incorporates free surface and ambient wave effects into a nonlinear parametric model. Subsequently its use is demonstrated via simulation of a scale model submarine manoeuvring under control of a nonlinear depth keeping control system in a sea way. An energy-based model is presented that represents the underactuated submarine in a free surface affected state. This model is then used to synthesize a control law using Port-Hamiltonian theory and interconnection and damping assignment passivity-based control. Lyapunov analysis is used to study stability of the closed-loop system, and a simulation-based demonstration illustrates the performance of the control law. The results demonstrate that a closed loop non-linear controller is able to improve the quality of near surface depth keeping by automatically compensating for parasitic effects in the hydrodynamics that can compromise depth keeping performance during manoeuvres.

1 Introduction

This paper presents a simulation model of a submarine maneuvering at periscope depth in waves, expounding upon the Lagrangian Nonlinear Manoeuvring and Seakeeping [LNMS] model proposed in [1], and explores the utility of this simulation model for the case of a controlled model scale submarine. The mathematical model is extended for practical application, parameters are identified, and a subset of the model is employed to synthesize a control law. Finally simulation results facilitate discussion of strengths and weaknesses of the approach adopted.

Many modern submarines spend a considerable amount of time at periscope depth, but this operational environment is the most difficult in which to achieve stability and control. This is particularly true for diesel electric submarines, that are required to breathe in air in order to operate. When wave activity is significant, it can be difficult for a human driver to hold constant depth, which is a requirement both for Intelligence, Surveillance and Reconnaissance [ISR] using periscope mounted sensors and for diesel operation. When conditions are rough, an autopilot is invaluable, however autopilot design for this scenario is very difficult.

The traditional approach to designing an autopilot for the near surface environment is to achieve a nominal trim condition for a given speed using water tanks, then to rely on the robustness of an autopilot to compensate both for variations in trim and for the effect of waves. Examples of attempts to address the wave rejection problem alone include the work of [2], [3], [4], [5],[6],[7],[8],[9],[10],[11],[12]. All of these examples utilise models for synthesis and simulation that feature less fidelity than the LNMS model described herein. In particular, in these examples the

[*]RMIT University, Melbourne, Vic, Australia (e-mail: francis.valentinis@rmit.edu.au)
[†]Aerospace Corporation, El Segundo, CA, 90245 USA (e-mail: thomas.a.battista@aero.org)
[‡]Kevin T. Crofton Department of Aerospace and Ocean Engineering, Virginia Tech, Blacksburg, VA, 24061 USA (e-mail: cwoolsey@vt.edu)

free surface suction is not considered at all, nor are nonlinear interactions between manoeuvring forces, wave forces and time dependent free surface suction effects. An underwater vehicle or submarine will experience a suction effect when close to the surface that is dependent on the draft, orientation and speed. Prior to the work in this paper series, all published work on nonlinear parametric models of submarine motion neglected this effect and relied on the assumption that the configuration of the ballast tanks of the boat[1] sufficiently compensates for the suction.

This paper results from a project that has sought to develop a mathematical model of the free surface that can be used as the basis of a control law for a submarine maneuvering at periscope depth. Until recently, there have been no published mathematical models that can effectively be used in this role. The historical attempts at developing a mathematical model unifying sea keeping and manoeuvring are described in [13]. All of the attempts defined therein treat the problem of amalgamating a linear sea keeping model to a manoeuvring model. These models are all designed with surface craft in mind, so they do not consider the free surface suction effect. Conversely, in work that considers models of the free surface suction, such as [14], the interplay between maneuvering hydrodynamics, the free surface suction and the waves is not considered.

As part of this initiative, we recently proposed a Lagrangian mathematical unified model of sea keeping and maneuvering that represents free surface forces, including those due to waves and boat manoeuvring hydrodynamics. This work was described for the first time in the PhD thesis of the second author [15]. Two parts of this model have been published outside of the thesis. In the first part, a memory free model is developed [16]. In the second publication, fluid memory in calm water conditions is added [17]. This third paper in the series intrinsically adds the wave effects to the model, facilitating the closure of the work with the first demonstration of simulation and control using the model.

There is a substantial body of work in the literature on nonlinear autopilot design for underwater vehicles using energy shaping. In [18], energy shaping for cross-track control on an underactuated plant is demonstrated. In [19], integral action and anti-windup are added to an energy shaping control law. In [20], energy shaping is demonstrated on a six degree of freedom underactuated vehicle model, resulting in passive dynamics. Nonlinear precision guidance of an underactuated vehicle system on a helical trajectory is described in [21]. More recently, in [22] we employ energy shaping nonlinear control for an underwater vehicle to mitigate the effects of ambient ocean waves. In [23], we consider nonlinear control of a model scale submarine in emergency ascent, an important piece of work as it demonstrates how to control the boat when it is in a non neutrally buoyant condition, which is typical for near surface operation.

The standard parametric model structure for a submarine or an underwater vehicle is well established in the literature, with most models being based on the work of Gertler and Hagen (see [24]). The work of extending these models to non-canonical Hamiltonian and Lagrangian form was facilitated by the work of Leonard (see [25]) but only for a neutrally buoyant vehicle. In that work, a reduction by Lie group symmetry (see [26]) is adopted to derive a Hamiltonian model of the dynamics of a vehicle with coincident centres of buoyancy and gravity. In a successive step, the equations of motion for the vehicle are modified to account for the fact that the centres are vertically separated on the body. Reduction is possible in this case because of the remaining symmetry in translation and in yaw, after the gravitational moment breaks the symmetry in pitch and roll (see [26]). Extensions to this work to facilitate energy based modeling of non neutrally buoyant vehicles in a Hamiltonian framework were presented in [23].

In [15] and [16], we present a Lagrangian manoeuvring model for a free surface affected manoeuvring

[1] As per the standard maritime convention, submarines are referred to as "boats".

vehicle. This work is extended in [17] by addition of memory effects. In that work, a model subset presentable in Hamiltonian form is also described. In [1], we combine these models with the method described in [27] to approximate the effects of an ambient wave field. This results in the LNMS model, which is a unified model of sea keeping and manoeuvring that represents all free surface forces that can be represented with potential flow assumptions. The model is representative in all conditions for which a linear free surface boundary condition is valid, e.g., non broaching conditions in deep water.

In this paper, we adapt the Hamiltonian subset of the LNMS model for use in autopilot design using the interconnection and damping assignment, passivity-based control (IDA-PBC) approach [28, 29]. The implementation and demonstration of this design is facilitated in part by a model system identification and consequent development of a simulation. The use of the LNMS model allows for a much higher fidelity representation of the manoeuvring dynamics in this condition than has ever been possible with a parametric model. Nonetheless, we acknowledge that there will still be unmodelled effects, particularly in shallow water or in conditions that are close to broaching. We also acknowledge that the steps necessary to adapt the model to IDA-PBC also add modelling inaccuracies. Moreover, in this work we assume that waves cannot be sensed or predicted in any way. By adapting elements of the LNMS model, we reduce modeling uncertainty, but do not remove it entirely. For this reason, a nonlinear control strategy that is inherently robust was sought.

Motion control designs for marine vehicles based on energy-related properties like passivity and dissipativity have been very successful due to their inherent robustness; see, for example, [30] and [31] and references therein. For a physical system, it is possible to formulate a mathematical model that highlights the dissipative properties of the system despite parametric uncertainty; and then a controller can be designed so that stability depends only on dissipativity properties (see [32]). There are two commonly cited frameworks for energy-based control, namely the method of controlled Lagrangians and the Port Hamiltonian System (PHS) framework. In their most general formulation, the two approaches have been shown to be equivalent (see [33]), although the original concept of controlled Lagrangians was restricted to a special class of systems with symmetry.

The design of the control laws in this paper represents an extension to the autopilot design presented in [23]. In that work, the classical dynamic model of a slender-hull underwater vehicle —see [24] and [31] – is extended to support mass variation, and is expressed as a PHS following [34]. A tracking control design is then considered based on energy shaping and damping assignment such that the closed-loop system retains a PHS form. This design achieves control of speed in the body fixed forward and vertical directions as well as attitude for roll, pitch and yaw. This autopilot inner loop is designed to be compatible with the guidance law developed in the first author's prior work [21], which facilitates six degree of freedom guidance in an inertial frame.The work presented in this paper follows a similar approach, with the exception that the mathematical model that is used for controller synthesis and testing is adapted to follow a similar form to the LNMS.

The submarine of interest in this work is controlled by means of a single aft propeller, four independently actuated stern planes configured in an X formation and a pair of coupled sail-mounted hydroplanes. With a vehicle of this kind, it is not possible to control yaw without affecting velocity in sway. It is however possible to control pitch independently to velocity in heave. The reason for this is that the hydroplanes provide additional independent actuation to the aft control surfaces in the vertical plane. As in the first author's previous work, the unactuated plant channel is not controlled, and a suppression of dynamics approach is used to completely remove the uncontrolled behavior from the target dynamics.

The resulting closed loop system is then simulated in order to demonstrate three things. First, we

show for the first time how the LNMS model can be used to create high fidelity simulations. Second, we present results that allow readers to compare the forces generated with the LNMS model to those acting on a traditional, deeply submerged model. Third, we provide results to demonstrate performance of the model-based control law. The results of this study are then considered, with a view to understand both the effectiveness of the simulation and the benefits that nonlinear control can give in manoeuvring during near surface operations.

The focus of all of this work is to demonstrate the LNMS model in a practical, representative application. By building a simulated example, the authors describe at each step the relevant challenges, solutions and opportunities that reveal themselves when applying this model to this application. The presentation of such an example makes this paper very distinct from all previous publications on LNMS, which were very theoretical in nature.

In summary, this paper makes the following contributions specific to the LNMS model:

- It is extended to incorporate wave effects.
- It is identified using traditional tools (RANS CFD, frequency domain sea keeping codes, towing tank experiments).
- It is adapted to facilitate nonlinear control law design.
- It is used to create high fidelity simulations.
- Its predictions are compared to a traditional deeply submerged model.

2 Dynamics of Underwater Vehicles

The model of the vehicle to be used in this work will be based on an extension of the authors' prior work (see [15],[16],[17]). The notation used to describe the vehicle dynamics equations follows the SNAME conventions that are also adopted in the latest edition of [31]. The notation is summarized in Table 1.

The model focuses on the rigid body dynamics and the hydrodynamic loads that influence the motion of the platform. Largely following the notation of [31], the following expression for the dynamics is obtained:

$$\dot{\boldsymbol{\eta}} = \mathbf{J}(\boldsymbol{\eta})\boldsymbol{\nu}, \tag{1}$$

$$\begin{aligned}&\mathbf{M}\left(\boldsymbol{\nu},\boldsymbol{\eta},t\right)\dot{\boldsymbol{\nu}} + \mathbf{C}\left(\boldsymbol{\nu},\boldsymbol{\eta},t\right)\boldsymbol{\nu} + \mathbf{D}\left(\boldsymbol{\nu},\boldsymbol{\eta},t\right)\boldsymbol{\nu} + \mathbf{L}_V\left(\boldsymbol{\nu},\boldsymbol{\eta}\right)\boldsymbol{\nu} + \mathbf{g}\left(\boldsymbol{\eta}\right)\\ &\quad + \int_0^t \boldsymbol{K}_M\left(\boldsymbol{\nu},\boldsymbol{\eta},\boldsymbol{\eta}\left(\tau\right),t-\tau\right)\boldsymbol{\nu}\left(\tau\right)d\tau\\ &\quad + \mathbf{M}_D\left(\boldsymbol{\nu},\boldsymbol{\eta},t\right)\dot{\boldsymbol{\nu}}_{\mathrm{f}} + \mathbf{C}_D\left(\boldsymbol{\nu},\boldsymbol{\eta},t\right)\boldsymbol{\nu}_{\mathrm{f}} + \mathbf{D}_D\left(\boldsymbol{\nu},\boldsymbol{\eta},t\right)\boldsymbol{\nu}_{\mathrm{f}} = \overset{c}{\boldsymbol{\chi}} + \overset{e}{\boldsymbol{\chi}},\end{aligned} \tag{2}$$

Here, $\boldsymbol{\nu}_{\mathrm{f}}$ is the space- and time-dependent wave field velocity that would occur at the origin of the body frame (and expressed in the body frame) if the body were absent. The matrix $\mathbf{J}(\boldsymbol{\eta})$ in (1) is a change of coordinates. In (2), the generalized mass matrix $\mathbf{M}\left(\boldsymbol{\nu},\boldsymbol{\eta},t\right) = \mathbf{M}_b + \mathbf{M}_I\left(\boldsymbol{\nu},\boldsymbol{\eta}\right) + \mathbf{M}_M\left(\boldsymbol{\nu},\boldsymbol{\eta},t\right) + \mathbf{M}_E\left(\boldsymbol{\nu},\boldsymbol{\eta},t\right)$ comprises the rigid-body mass, instantaneous impulsive response added mass, memory affected added mass and external forcing added mass. The Coriolis-centripetal matrix $\mathbf{C}\left(\boldsymbol{\nu},\boldsymbol{\eta},t\right) = \mathbf{C}_b + \mathbf{C}_I\left(\boldsymbol{\nu},\boldsymbol{\eta}\right) + \mathbf{C}_M\left(\boldsymbol{\nu},\boldsymbol{\eta},t\right) + \mathbf{C}_E\left(\boldsymbol{\nu},\boldsymbol{\eta},t\right)$ consists likewise of Coriolis-centripetal contributions due to the rigid body alone, instantaneous impulsive response, memory effects, and external forcing. The damping matrix $\mathbf{D}\left(\boldsymbol{\nu},\boldsymbol{\eta},t\right) = \mathbf{D}_V\left(\boldsymbol{\nu},\boldsymbol{\eta}\right) + \mathbf{D}_I\left(\boldsymbol{\nu},\boldsymbol{\eta}\right) + \mathbf{D}_M\left(\boldsymbol{\nu},\boldsymbol{\eta},t\right) + \mathbf{D}_E\left(\boldsymbol{\nu},\boldsymbol{\eta},t\right)$

Table 1: Summary of marine craft motion variables.

Variable	Name	Frame	Units
n	North position	Earth-fixed	m
e	East position	Earth-fixed	m
d	Down position	Earth-fixed	m
ϕ	Roll angle	-	rad
θ	Pitch angle	-	rad
ψ	Yaw angle	-	rad
u	Velocity in direction of surge force	Body-fixed	m/s
v	Velocity in direction of sway force	Body-fixed	m/s
w	Velocity in direction of heave force	Body-fixed	m/s
p	Roll rate	Body-fixed	rad/s
q	Pitch rate	Body-fixed	rad/s
r	Yaw rate	Body-fixed	rad/s
X	Force in direction of surge	Body-fixed	rad/s
Y	Force in direction of sway	Body-fixed	rad/s
Z	Force in direction of heave	Body-fixed	rad/s
K	Moment in direction of roll	Body-fixed	rad/s
M	Moment in direction of pitch	Body-fixed	rad/s
N	Moment in direction of yaw	Body-fixed	rad/s
O	Reference point on the body	Body-fixed	-
N_e	Reference point on the Earth	Earth-fixed	-
$\mathbf{p}^n_{O/N_e} = [n,\, e,\, d]^\top$	Position vector	Earth-fixed	-
${}^n\dot{\mathbf{p}}^b_{O/N_e} = [u,\, v,\, w]^\top$	Linear-velocity vector	Body-fixed	-
$\boldsymbol{\Gamma} = [\Gamma_1, \Gamma_2, \Gamma_3]^\top$	Tilt vector	Body-fixed	-
$\boldsymbol{\omega}^b_{b/n} = [p, q, r]^\top$	Angular-velocity vector	Body-fixed	-
$\boldsymbol{\eta} = [(\mathbf{p}^n_{O/N_e})^\top, \boldsymbol{\Gamma}^\top, \psi]^\top$	Generalized position vector	Earth Fixed	-
$\boldsymbol{\nu} = [({}^n\dot{\mathbf{p}}^b_{O/N_e})^\top, (\boldsymbol{\omega}^b_{b/n})^\top]^\top$	Generalized velocity vector	Body-fixed	-
m	mass		kg
b	buoyancy		N
g	gravity		m/s^2

consists of viscous damping, instantaneous impulsive response damping, memory affected damping and external forcing damping. The vector $\mathbf{L}_V(\boldsymbol{\nu}, \boldsymbol{\eta})$ consists of non-potential lift-like effects while the vector $\mathbf{g}(\boldsymbol{\eta})$ represents restoring forces due to gravity and buoyancy.

The memory effect matrix $\boldsymbol{K}_M$ incorporates the fluid memory incurred by the vehicle motion near a free surface. Both the subscript E (external forcing) terms and the D (disturbance) terms arise due to the presence of external flow effects (e.g. waves). We choose to separate the contributions as follows: the subscript D terms capture any external flow-induced forcing for a vehicle which is either fixed or moving, while the subscript E terms capture external flow-induced forcing for a vehicle which is moving. More specifically, the E terms can be thought of as modifications to the calm water terms – e.g., the presence of an external flow field would alter the added mass, damping, and surface suction terms. Crook [35] talks about modifications to the surface suction due to the presence of an external wave field, so effects like this would be included here. Essentially these terms capture any effects due to coupled vehicle motion and external flow. The D terms, by contrast, will persist even if the vehicle motion were arrested. So for instance, if a vehicle were held fixed by some mechanism in a wave field, these terms would capture the hydrodynamic forces acting on the stationary vehicle. In the subsequent sections, the terms which appear in the equations of motion are described in more detail. The vector $\boldsymbol{\chi}$ represents the control forces. $\overset{\mathrm{c}}{\boldsymbol{\chi}}$ is the vector of control forces in the actuated degrees of freedom that are induced by the action of the control system, whereas $\overset{\mathrm{e}}{\boldsymbol{\chi}}$ is likewise a vector of forces affecting only the unactuated degrees of freedom.

The latter results from the action of the control system but is essentially a disturbance.

2.1 Rigid Body and Hydrostatic Dynamics

We follow the same approach as in [23] in building the equations of motion for the rigid body. In that work, the starting point is the elaboration of Fossen's model [31], but modifications are made to accommodate the use of a unit tilt vector paired with the heading as the orientation vector $\boldsymbol{\eta}_2 = [\Gamma_1, \Gamma_2, \Gamma_3, \psi]^\top$. This representation follows the work of Valentinis and Woolsey [23]. Fossen's definition of $\boldsymbol{\eta}_1 = [x, y, z]^\top$ remains unchanged.

Following the definitions of Leonard (see [25]), $\boldsymbol{\Gamma} = [\Gamma_1, \Gamma_2, \Gamma_3]^\top$, where $\Gamma_1 = -\sin(\theta)$, $\Gamma_2 = \cos(\theta)\sin(\phi)$ and $\Gamma_3 = \cos(\theta)\cos(\phi)$. Conversely, $\theta = -\arcsin(\Gamma_1)$ and $\phi = \arctan\left(\frac{\Gamma_2}{\Gamma_3}\right)$.

Fossen defines the matrix $\mathbf{J}(\boldsymbol{\eta}_2) = \text{diag}([\mathbf{J}_1(\boldsymbol{\eta}_2), \mathbf{J}_2(\boldsymbol{\eta}_2)])$ as the matrix that rotates the body frame to the inertial frame. This matrix must be modified in order to facilitate use of the new orientation vector $\boldsymbol{\eta}_2$. The new matrix is defined in three components:

$$\mathbf{J}(\boldsymbol{\eta_2}) = \begin{bmatrix} \mathbf{J}_1(\boldsymbol{\eta}_2)^T & \mathbf{0} & \mathbf{0} \\ \mathbf{0} & \mathbf{J}_2(\boldsymbol{\eta}_2)^T & \mathbf{J}_3(\boldsymbol{\eta}_2)^T \end{bmatrix}^\top \tag{3}$$

where $\mathbf{J}_1(\boldsymbol{\eta}_2)$ maps $\boldsymbol{\nu}_1$ to $\dot{\boldsymbol{\eta}}_1$ and where $\mathbf{J}_2(\boldsymbol{\eta}_2)$ and $\mathbf{J}_3(\boldsymbol{\eta}_2)$ map $\boldsymbol{\nu}_2$ to $\dot{\boldsymbol{\eta}}_2$. To express $\mathbf{J}_1$, the definition of Fossen is used with substitutions for θ and ϕ in terms of $\boldsymbol{\Gamma}$.

$$\mathbf{J}_1(\boldsymbol{\eta}_2) = \begin{bmatrix} \xi_1\psi_1 & -\frac{\Gamma_1\Gamma_2\psi_1}{\Gamma_3\xi_2} - \frac{\psi_2}{\xi_2} & -\frac{\Gamma_1\psi_1}{\xi_2} + \frac{\Gamma_2\psi_2}{\Gamma_3\xi_2} \\ \xi_1\psi_2 & \frac{\psi_1}{\xi_2} - \frac{\Gamma_1\ \Gamma_2\psi_2}{\Gamma_3\xi_2} & -\frac{\Gamma_2\psi_1}{\Gamma_3\xi_2} - \frac{\Gamma_1\psi_2}{\xi_2} \\ \Gamma_1 & \frac{\Gamma_2\xi_1}{\Gamma_3\ \xi_2} & \frac{\xi_1}{\xi_2} \end{bmatrix} \tag{4}$$

where $\psi_1 = \cos(\psi)$, $\psi_2 = \sin(\psi)$, $\xi_1 = \sqrt{1-\Gamma_1^2}$ and $\xi_2 = \sqrt{\frac{\Gamma_2^2+\Gamma_3^2}{\Gamma_3^2}}$.

Conveniently, $\dot{\boldsymbol{\Gamma}} = \boldsymbol{\Gamma} \times \boldsymbol{\nu}_2 = \hat{\boldsymbol{\Gamma}}\boldsymbol{\nu}_2$, where the $\hat{\cdot}$ operator signifies the cross product-equivalent matrix. This allows for a very straight forward definition of $\mathbf{J}_2(\boldsymbol{\eta}_2)$, which maps $\boldsymbol{\nu}_2$ to $\dot{\boldsymbol{\Gamma}}$:

$$\mathbf{J_2}(\boldsymbol{\eta}_2) = \hat{\boldsymbol{\Gamma}} \tag{5}$$

The definition of $\mathbf{J}_3(\boldsymbol{\eta}_2)$, which maps $\boldsymbol{\nu}_2$ to $\dot{\psi}$, follows [1]:

$$\mathbf{J_3}(\boldsymbol{\eta}_2) = \frac{1}{1-\Gamma_1^2}\boldsymbol{\Gamma}^\top \hat{\mathbf{e}}_3\hat{\mathbf{e}}_1 \tag{6}$$

where $\mathbf{e_1} = [1,0,0]^\top$ and $\mathbf{e_3} = [0,0,1]^\top$.

Extending the work of Leonard, the restoring forces can then be expressed as

$$\mathbf{g}(\boldsymbol{\eta}) = \mathbf{J}(\boldsymbol{\eta_2})^\top \begin{bmatrix} \mathbf{e_3}(mg-b) \\ b\mathbf{p}^{\mathbf{b}}_{\mathbf{B/O}} - mg\mathbf{p}^{\mathbf{b}}_{\mathbf{G/O}} \\ 0 \end{bmatrix} \tag{7}$$

where $\mathbf{p}^b_{G/O} = [x_G, y_G, z_G]^\top$ is the center of gravity vector with respect to the reference point O. In this model, the point O corresponds to the fixed centre of buoyancy. The magnitude of the buoyancy force is denoted b.[2]

2.2 Hydrodynamic Forces

The model of the manoeuvring hydrodynamics adopted in this work is a total flow model, i.e., it represents both viscous and potential effects. The model as a whole is time dependent, and includes a representation of incident wave effects. It would be convenient to present the model as an addendum to existing open literature models (i.e., as additional terms), however this is not possible. The LNMS approach models all potential forces for all depths, including the deep submerged depths. Rather than dividing the model into free surface and deeply submerged terms, we model non-potential effects[3] and potential effects separately.

2.2.1 Non-potential Effects

Having at least a basic model of non-potential forces is critical to achieving realistic simulation outcomes. Without such a model, prediction of steady state sailing forces and moments is not possible. The focus of this work is demonstrating the LNMS model, so herein our objective is to demonstrate how to integrate and represent a model of the non-potential forces in the context of an LNMS model. Like others [35], we make the assumption that wave effects are a purely potential phenomenon. Likewise, we employ an elementary model of the depth dependent viscous contributions.

Unlike the potential terms in the model, which arise from an analytical derivation, the starting point for the derivation of the non-potential model must be a model that accurately predicts the total (i.e. potential + non-potential) forces in a critical set of contexts. In this work, we consider two: all manoeuvring conditions in the deeply submerged state, and straight and level sailing at a variety of depths.

Consideration of the former case is critical in order to allow the model to recover the regular deeply submerged model typically found in the literature as the depth increases. The latter is critical for representing changes in trim as a function of depth, which is extremely important for submarine simulation and control.

The process we will adopt to characterise these non-potential effects will commence with a model of familiar form for the total (potential + non-potential) flow. From this total flow model (which we will identify at a variety of depths and speeds), we will subtract the action of the LNMS model in order to isolate the non-potential terms. When the resulting non-potential model is added to the LNMS model, the correct (i.e., total flow) characteristics will result. Our starting point is therefore the presentation of a model of the total forces.

In the typical representations found in the literature, the manoeuvring hydrodynamic forces acting on a deeply submerged submarine (i.e., where all free surface interaction effects are negligible) can be represented as a summation of polynomials in the velocity components, where the polynomial coefficients depend on the body geometry. Examples of such representations include that of Gertler and Hagen [24] and Feldman [36].

[2]The use of a fixed centre of buoyancy introduces a limitation that restricts the model from being used in a surfaced or broaching state.

[3]In this work, we use the term 'non-potential effects' to aggregate viscous effects and circulation effects that are not represented by a potential flow model.

We take the same approach to represent the deeply submerged submarine. The hydrodynamic forces for a deeply submerged body are then represented by the product $\mathbf{H}(\boldsymbol{\nu})\boldsymbol{\nu}$ where the matrix function $\mathbf{H}(\boldsymbol{\nu})$ captures the nonlinearity of these effects. In the models of Gertler and Hagen, as well as others used in the submarine hydrodynamics community, the fluid forces consist of a combination of potential and non-potential forces in the deeply submerged environment. For this model, we choose to separate the non-potential from the potential effects.

$$\mathbf{H}(\boldsymbol{\nu}) = \begin{pmatrix} X_{uu}u & X_{vr}r+X_{vv}v & X_{wq}q+X_{ww}w & X_{rp}r & X_{qq}q & X_{rr}r \\ Y_pp+Y_rr & Y_{vr}r+Y_vu+Y_{v|v|}\sqrt{v^2+w^2} & 0 & Y_{pq}q+Y_{wp}w & 0 & Y_{r|r|}|r| \\ Z_qq & Z_{vp}p+Z_{vr}r+Z_{vv}v & Z_wu+Z_{w|w|}\sqrt{v^2+w^2}+Z_{w|q|}|q| & Z_{pp}p & Z_{q|q|}|q| & Z_{rr}r \\ K_rr+K_vv & K_{v|v|}\sqrt{v^2+w^2} & 0 & K_pu+K_{wp}w & K_{qr}r & K_{r|r|}|r| \\ M_ww & M_{vr}r+M_{vv}v & M_{w|w|}\sqrt{v^2+w^2} & M_{rp}r & M_{q|q|}|q|+M_qu & M_{rr}r \\ N_pp+N_vv & N_{v|v|}\sqrt{v^2+w^2} & 0 & N_{pq}q & 0 & N_{r|r|}|r|+N_ru+N_{rv}v \end{pmatrix} \tag{8}$$

The product $\mathbf{H}(\boldsymbol{\nu})\boldsymbol{\nu}$ is only representative of the forces experienced in a deeply submerged state. Other effects due to interaction with the free surface are not represented, but are added later through the terms of the LNMS model, which effectively replace the potential terms in the product $\mathbf{H}(\boldsymbol{\nu})\boldsymbol{\nu}$ with terms that will represent the forces experienced in both the deeply submerged and free surface affected conditions.

As the submarine nears the free surface, it will experience an additional combination of potential and non-potential forces. For this work, we assume that the viscous effects due to free surface interactions are not negligible, as they play a significant part in simulating the boat. This model does not, however, account for viscous effects due to incident waves as we assume that these forces are dominated by potential effects. This modelling assumption was initially motivated by standard practice in surface craft manoeuvring analysis, for which it is typical to use potential flow based codes. Others, including Crook [35] made similar assumptions. In later phases of this project, this assumption was corroborated through correlation of towing tank results. A careful characterisation of the viscous effects due to incident waves would be interesting to investigate, but we defer this to future work.

The term $\mathbf{H}(\boldsymbol{\nu})\boldsymbol{\nu}$ is used as the basis for the determination of the matrices $\mathbf{D}_V$ and $\mathbf{L}_V$ for deeply submerged conditions. To determine these values, we exploit the following properties:

$$\mathbf{H}(\boldsymbol{\nu})\boldsymbol{\nu} = \mathbf{C}_I(\boldsymbol{\nu}, \boldsymbol{\eta}|_{d\to\infty})\boldsymbol{\nu} + \mathbf{L}_V(\boldsymbol{\nu}, \boldsymbol{\eta}|_{d\to\infty})\boldsymbol{\nu} + \mathbf{D}_V(\boldsymbol{\nu}, \boldsymbol{\eta}|_{d\to\infty})\boldsymbol{\nu} + \mathbf{D}_I(\boldsymbol{\nu}, \boldsymbol{\eta}|_{d\to\infty})\boldsymbol{\nu} \tag{9}$$

where $\mathbf{D}_V$ is strictly diagonal and $\mathbf{L}_V$ contains the off-diagonal terms of the non-potential effects when deeply submerged.

In shallow but calm water, the free surface suction forces experienced by a submarine will have a viscous as well as a potential component. As a result, $\mathbf{D}_V$ and $\mathbf{L}_V$ are strictly functions of both $\boldsymbol{\nu}$ and $\boldsymbol{\eta}$.

2.2.2 Potential effects

As discussed in [37] and [15], the calm-water fluid response to vehicle motion can be broken into an *impulsive* response and a *memory* response. The interactions between the vehicle and the

surrounding fluid can be characterized by an energy-like *Lagrangian* function:

$$\begin{aligned}\mathcal{L} = &\frac{1}{2}\boldsymbol{\nu}^T\big(\boldsymbol{M}_{\mathrm{b}} + \boldsymbol{M}_{\mathcal{B}} + \Delta\boldsymbol{M}_{\mathcal{B}}(\boldsymbol{\eta}) + \boldsymbol{M}_{\mathcal{S}_0}(\boldsymbol{\eta},\boldsymbol{\nu})\big)\boldsymbol{\nu} \\ &+ \boldsymbol{\nu}^T\int_0^t \left[\boldsymbol{K}_{\mathcal{B}}(\boldsymbol{\eta}(\tau), t-\tau) + \boldsymbol{K}_{\mathcal{S}_0}(\boldsymbol{\eta},\boldsymbol{\nu},\boldsymbol{\eta}(\tau), t-\tau)\right]\boldsymbol{\nu}(\tau)d\tau \end{aligned} \tag{10}$$

A formal derivation of (10) using potential flow theory appears in [15] and [17]. Briefly, $\boldsymbol{\nu}^T\boldsymbol{M}_{\mathrm{b}}\boldsymbol{\nu}/2$ accounts for the rigid body kinetic energy, $\boldsymbol{\nu}^T\boldsymbol{M}_{\mathcal{B}}\boldsymbol{\nu}/2$ accounts for the deeply submerged impulsive fluid kinetic energy (absent the free surface), and $\boldsymbol{\nu}^T\Delta\boldsymbol{M}_{\mathcal{B}}\boldsymbol{\nu}/2$ corrects the deeply submerged impulsive fluid kinetic energy to account for rigid body motion near a rigid surface. The term $\boldsymbol{\nu}^T\boldsymbol{M}_{\mathcal{S}_0}\boldsymbol{\nu}/2$ then corrects the system energy to account for the impulsive energy stored within a deformable free surface. The convolution terms $\boldsymbol{K}_{\mathcal{B}}$ and $\boldsymbol{K}_{\mathcal{S}_0}$ appearing in (10) account for the ensuing memory effects which govern the wave resistance forces. The Lagrangian expression (10) can be used to generate a nonlinear version of the Cummins equations [37]; see [15].

The Lagrangian function can be augmented using the approach outlined in [27] to account for external wave excitation forces:

$$\begin{aligned}\mathcal{L} = &\frac{1}{2}\left(\boldsymbol{\nu} - \boldsymbol{\nu}_{\mathrm{f}}(\boldsymbol{\eta},t)\right)^T\left(\boldsymbol{M}_{\mathrm{b}} + \boldsymbol{M}_{\mathcal{B}} + \Delta\boldsymbol{M}_{\mathcal{B}}(\boldsymbol{\eta}) + \boldsymbol{M}_{\mathcal{S}_0}(\boldsymbol{\eta},\boldsymbol{\nu})\right)\left(\boldsymbol{\nu} - \boldsymbol{\nu}_{\mathrm{f}}(\boldsymbol{\eta},t)\right) \\ &+ \boldsymbol{\nu}^T\int_0^t \left[\boldsymbol{K}_{\mathcal{B}}(\boldsymbol{\eta}(\tau), t-\tau) + \boldsymbol{K}_{\mathcal{S}_0}(\boldsymbol{\eta},\boldsymbol{\nu},\boldsymbol{\eta}(\tau), t-\tau)\right]\boldsymbol{\nu}(\tau)d\tau \end{aligned} \tag{11}$$

Again, we point the reader to [15] for a formal derivation of (11). Briefly, the key difference between (10) and (11) is that we replace $\boldsymbol{\nu}$ in the top line of (10) with the vehicle external flow-relative velocity $\boldsymbol{\nu} - \boldsymbol{\nu}_{\mathrm{f}}$. In this context, hydrodynamic forces due to external flow effects are generated by a simple modification to the underlying system Lagrangian function. The contributions to (2) from the potential-driven effects are generated from this Lagrangian function using a modified version of the Euler-Lagrange equations [15]:

$$\frac{d}{dt}\frac{\partial\mathcal{L}}{\partial\boldsymbol{\nu}} + \begin{pmatrix} \widehat{\boldsymbol{\omega}^b_{b/n}} & \boldsymbol{0} \\ \widehat{{}^n\dot{\mathbf{p}}^b_{O/N}} & \widehat{\boldsymbol{\omega}^b_{b/n}} \end{pmatrix}\frac{\partial\mathcal{L}}{\partial\boldsymbol{\nu}} - \boldsymbol{J}(\boldsymbol{\nu})^T\frac{\partial\mathcal{L}}{\partial\boldsymbol{\eta}} = \boldsymbol{0} \tag{12}$$

As the process to generate the hydrodynamic terms is a cumbersome one, we elect to place the explicit expressions resulting from applying (12) to (11) in Appendix 9.

2.3 Hydrodynamic Actuation

For the vehicle considered in this paper, the vector of control forces has the following form:

$$\overset{\mathrm{c}}{\boldsymbol{\chi}} = \begin{bmatrix} \overset{\mathrm{c}}{\chi}_u & \overset{\mathrm{c}}{\chi}_v & \overset{\mathrm{c}}{\chi}_w & \overset{\mathrm{c}}{\chi}_p & \overset{\mathrm{c}}{\chi}_q & \overset{\mathrm{c}}{\chi}_r \end{bmatrix}^\top \tag{13}$$

The elements of this vector are not independently assignable. In particular, the force in the sway direction $\overset{\mathrm{c}}{\chi}_v$ is a consequence of the effective rudder deflection whose purpose is to generate the yaw control moment $\overset{\mathrm{c}}{\chi}_r$.

The actuator configuration of the vehicle consists of thrust force due to the revolution of a propeller δ_{RPM}, a coupled hydroplane pair mounted on the sail [4], whose deflection is denoted δb, and four

[4] We use the term "sail" to describe the hydrofoil shaped structure that traditionally houses the periscope. This is sometimes known as the "fin" or "fairwater". We distinguish this from a "casing", which is a deck-like structure covering pipework that is laid over the top of the pressure hull

fins at the stern in an X configuration. Looking at the vehicle from the stern end, the fins are numbered in the clockwise direction from 1 to 4 starting with the upper port side. These deflections are denoted δ_{X1}, δ_{X2}, δ_{X3}, δ_{X4}. The actuator variables are mapped to the forces they generate through the following actuator configuration function:

$$\overset{\mathbf{c}}{\boldsymbol{\chi}} = \mathbf{B}\left(\boldsymbol{\nu}, \boldsymbol{\delta}\right) \tag{14}$$

where

$$\boldsymbol{\delta} \triangleq \begin{bmatrix} \delta_{RPM} \\ \delta_{X1} \\ \delta_{X2} \\ \delta_{X3} \\ \delta_{X4} \\ \delta_b \end{bmatrix} \quad \text{and} \quad \mathbf{B}\left(\boldsymbol{\nu}, \boldsymbol{\delta}\right) \triangleq u^2 \begin{bmatrix} X_{\delta_{X1}}\delta_{X1} & X_{\delta_{X2}}\delta_{X2} & X_{\delta_{X3}}\delta_{X2} & X_{\delta_{X4}}\delta_{X3} & X_{\delta_b}\delta_b \\ Y_{\delta_{X1}} & Y_{\delta_{X2}} & Y_{\delta_{X3}} & Y_{\delta_{X4}} & Y_{\delta_b} \\ Z_{\delta_{X1}} & Z_{\delta_{X2}} & Z_{\delta_{X3}} & Z_{\delta_{X4}} & Z_{\delta_b} \\ K_{\delta_{X1}} & K_{\delta_{X2}} & K_{\delta_{X3}} & K_{\delta_{X4}} & K_{\delta_b} \\ M_{\delta_{X1}} & M_{\delta_{X2}} & M_{\delta_{X3}} & M_{\delta_{X4}} & M_{\delta_b} \\ N_{\delta_{X1}} & N_{\delta_{X2}} & N_{\delta_{X3}} & N_{\delta_{X4}} & N_{\delta_b} \end{bmatrix} \begin{bmatrix} \delta_{X1} \\ \delta_{X2} \\ \delta_{X3} \\ \delta_{X4} \\ \delta_b \end{bmatrix} + \begin{bmatrix} X_p \\ 0 \\ 0 \\ K_p \\ 0 \\ 0 \end{bmatrix} \tag{15}$$

In this representation of the actuator configuration, the terms due to deflection of the fins are standard[5]. In this equation structure we permit asymmetries in the values of all control surface coefficients, however for the particular simulation example presented in this work we implement some symmetries (see eqn. 61).The terms X_p and K_p represent the propeller thrust and torque. The propeller is modeled following standard practice (see [31] for an explanation and for definitions of the terms used below), and the thrust and torque coefficients are modeled as second order polynomials[6] as follows:

$$n_p = \frac{\delta_{RPM}}{60.0} \tag{16}$$

$$X_p = D_p^4 n_p^2 K_t \left(1 - t_p\right) \rho \tag{17}$$

$$J_p = \frac{u\left(1 - w_t\right)}{D_p n_p} \tag{18}$$

$$K_t = K_{t1} + K_{t2} J_p + K_{t3} J_p^2 \tag{19}$$

$$K_q = K_{q1} + K_{q2} J_p + K_{q3} J_p^2 \tag{20}$$

$$K_p = -D_p^5 n_p^2 K_q \rho \tag{21}$$

3 Suitability of the Proposed Model for Control Design

In the context of model-based control design, having a representative set of model parameters is essential for assessing control performance and system stability. A significant effort went into adapting the equations of motion (2) for simulation and ultimately control design. The Joubert BB2 submarine had already been the subject of analysis by hydrodynamics research teams for many years and the data from some of these initiatives proved valuable as a starting point for a model identification effort. In particular, BB2 data came from experiments jointly conducted by DST group and the Australian Maritime College (AMC) and high fidelity Reynolds-averaged Navier-Stokes (RANS) computational fluid dynamics (CFD) simulation. Data from the panel code ShipMo3D, developed by Defence Research and Development Canada (DRDC), was also used to identify certain terms in the equations of motion which arise from potential flow effects. In the

[5] In all cases, positive control surface deflections result in a negative force in the Z direction (i.e up)

[6] In this study, different polynomials were used for the forward and astern operational quadrants.

main text, we choose to provide only a high level summary of how these data sets were used to populate the system model and corroborate the results with lab experiments; we provide citations where appropriate and note that the reader can find a more extensive overview of this process in Appendix 10.

3.1 System Identification

With this work, one of the authors' primary objectives is to demonstrate how the LNMS model is used in a practical application. Identification, adaptation of the model to controls design, and simulation are challenging, but the potential benefits – high-performance control, real-time simulation, model-based estimation, etc. – justify discussion of a rich tutorial example. The starting point for such an example is the identification of the total flow model.

Following the development of an identified model, we create simulations that can be used for corroboration of predictions with available data - in this case CFD simulations and towing tank experiments. In an ideal project scenario, this would be followed by testing and tuning with a free running model. This latter step was outside of scope for work reported herein, however. In any case, having incorporated the most realistic information available to support this discussion it will be possible to describe how the LNMS model can be used for control design and closed-loop motion simulation. First, though, we summarise the identification process, and the process used to corroborate fluid flow study results with model predictions.

System identification was carried out in two phases. These two are described in greater detail in Appendix 10. Firstly, the deeply submerged model parameters, including added mass terms, viscous terms, and circulation-induced terms, were identified. RANS CFD simulations were primarily used for this, however DRDC ShipMo3D was used for the deeply submerged added mass. The resulting deeply submerged parameter set is identical to the model presented by the first and third author in [23]. The second phase of system identification is more extensive and targets the near-surface potential flow and viscous model terms. For the potential flow terms, the principal idea is that all terms appearing in the equations of motion derive from the Lagrangian function (11). If the matrices $\Delta\boldsymbol{M}_{\mathcal{B}}$, $\boldsymbol{M}_{\mathcal{S}0}$, $\boldsymbol{K}_{\mathcal{B}}$, and $\boldsymbol{K}_{\mathcal{S}0}$ can be identified for a variety of depths and speeds, one can predict the corresponding hydrodynamic forces. The fact that the same set of parameters can be identified for both maneuvering in calm water and maneuvering in waves is one strength of the LNMS model.

One recently developed approach for identifying the LNMS model comes from Jung [38]. (Also see [39].) In that dissertation, a systematic approach to characterising the instantaneous impulsive response and memory terms is presented. To facilitate that, a modified version of the LNMS model was created that could be identified directly using output from a specially modified version of the time domain sea keeping code AEGIR. In our opinion, this approach results in the best known characterisation of the LNMS model. The development of the identification approach used in this effort, however, predates the work of Jung and has not been previously published. This approach uses tools more readily available to many readers and still follows the principal underlying assumptions outlined by Jung. Namely, we assume that the matrices $\boldsymbol{M}_{\mathcal{S}0}$ and $\boldsymbol{K}_{\mathcal{S}0}$ are both zero. From [38], these assumptions are consistent with how standard panel and other potential flow codes resolve the free surface boundary conditions. Moreover, the results from the simulation and experimentation tasks conducted as part of this work lead us to believe that these simplifying assumptions are reasonable, because there has been no significantly negative impact on the model's ability to represent the potential contributions to either steady state free surface affected forces or induced wave response.

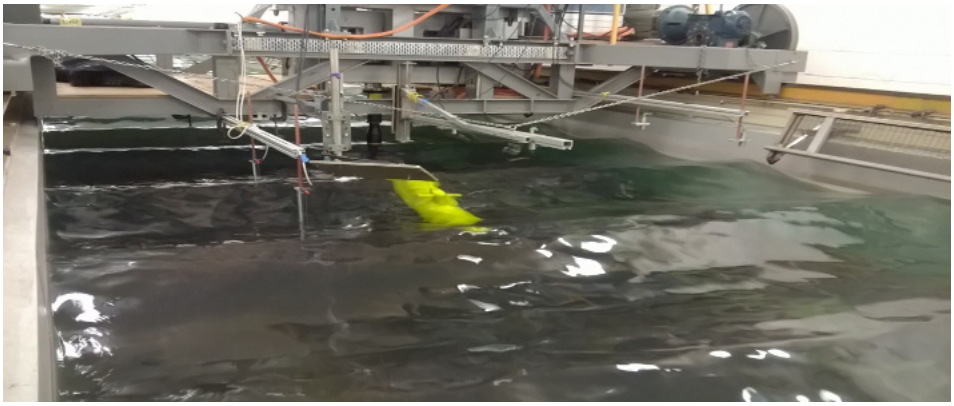

Figure 1: Photograph of AMC tow tank test in progress

For the approach adopted in this work, identification of the near-surface terms that can be represented with potential flow (i.e., the LNMS model) was undertaken primarily by the panel code ShipMo3D. The principal challenge is that all of the near-surface terms depend on the vehicle depth, orientation, and forward speed, which makes identification purely from high-fidelity CFD (e.g., RANS) tedious and often time-prohibitive. Leveraging RANS CFD results also presents a separate challenge: viscous and rotational flow effects must be subtracted from the results when populating the LNMS potential flow terms. Thus, we choose to leverage the lower-fidelity panel code ShipMo3D to handle the bulk of the parameter identification for LNMS itself, and use results from a subset of RANS CFD runs to identify the non-potential terms that are critical for prediction of free surface suction in undisturbed conditions. Additional details on the RANS CFD simulations can be found in Appendix 10 and in [40]. Towing tank testing proved important in helping to both fine tune and verify the balance between the potential effects (characterized primarily with ShipMo3D) and the viscous contributions (that were identified primarily with CFD). This is important because without this the authors were unable to isolate the viscous from non viscous effects from the CFD results.

3.2 Corroboration of Fluid Flow Simulations and Experiments with Reduced Order Simulation of Identified Model

In order to corroborate identified model predictions with fluid dynamics studies, a Matlab implementation of the full model was developed for two operating conditions of interest. The first was for the BB2 moving with a constant forward speed and at a constant depth near the surface. This case serves to corroborate model predictions with CFD simulations of this scenario. The forces and moments recorded from this study are reproduced in Table 2, which illustrates the magnitude of forces and moments that need to be modeled by the total flow model for simulation of undisturbed conditions. The second case is a simulation of a towing tank experiment with a towed captive model. This simulation served to corroborate the identified model predictions with the tow tank experiments of the BB2 under waves conducted at the AMC towing tank; a photograph of the test apparatus is shown in Figure 1.

The towing tank results are post processed with the SMOO filter from SIDPAC [41]. Figure 2 shows results for pitch moment (M), and forces in heave (Z), and surge (X). Wave height in mm is denoted (W) and is measured by a stationary sensor at the wavemaker, unlike other sensors which

are fixed to the model.[7] The wavemaker is set to produce a wave of 0.1m amplitude at a frequency of 0.84 Hz, resulting in wavelength of 2.2m. The results suggest that the predictions of the total flow model for the forces are slightly greater in magnitude than the measured forces, but within the uncertainty of the experiment. Likewise the moment is slightly under predicted, but also within the experimental uncertainty.

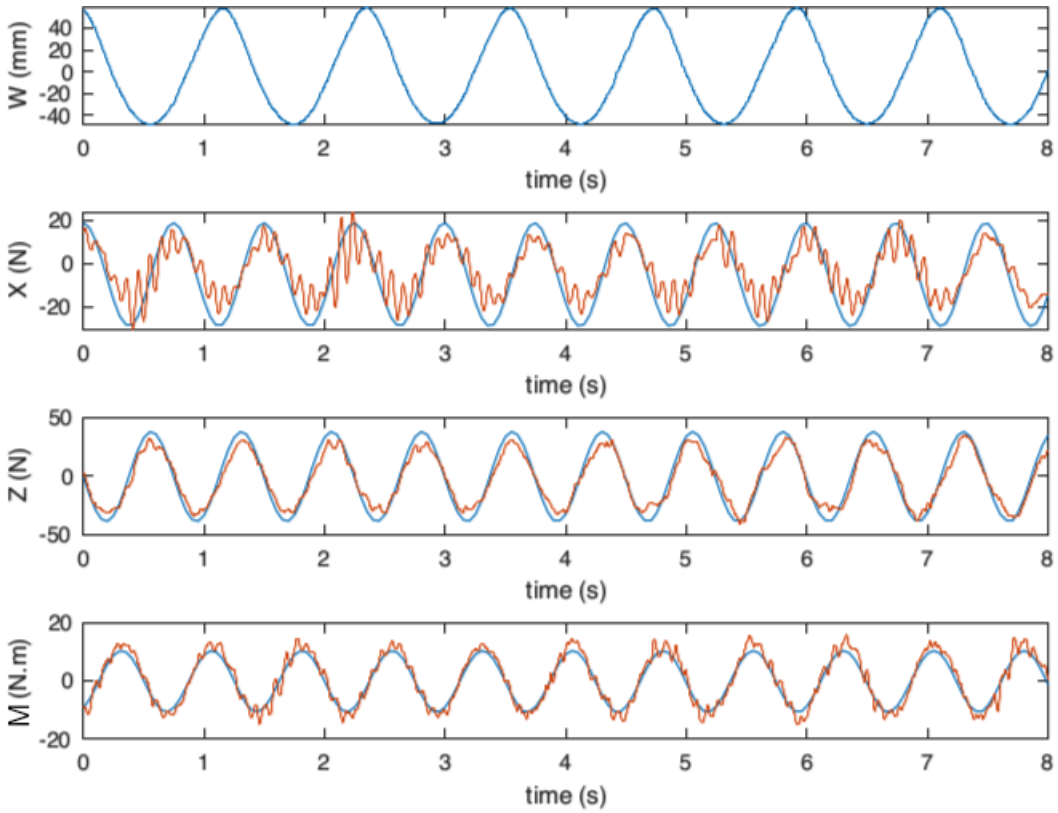

Figure 2: Comparison of total flow model with tow tank test results (W is the wave height, X, Z are forces in surge and heave, M is pitching moment). SMOO Filtered results are shown in red.

The total flow model was implemented in the Matlab Simulink environment initially as a three degree of freedom simulation. A practical challenge with implementing the LNMS terms in the model is the numerous gradient terms. For this study, in the case of the majority of these terms, we used finite differencing on-line to calculate the values of the gradients. An exception to this was the terms identified with the CFD analysis. In these cases ($\Delta\mathbf{M}_{\mathcal{B}11}$, $\Delta\mathbf{M}_{\mathcal{B}13}$, $\Delta\mathbf{M}_{\mathcal{B}31}$), lookup tables were used to define both the mass matrix values and the values of the gradients with respect to depth. The authors found that without this stored gradient information, precise prediction of the free surface suction effects was not possible.

In order to numerically replicate the towing tank test scenario, the simulation was configured for a constant wave amplitude and frequency matching the test. In real world conditions, a submarine will experience steady state (i.e., mean) free surface suction forces that are a function of sea state as well as velocity, depth and orientation [35]. The correct representation of the sea state dependency required attention in the simulation. LNMS is a nonlinear model, however its derivation relies on

[7] A difference in measurement between the wavemaker sensor measured frequency and body measured quantities is observed

a linearised free surface boundary condition. As a result of this, second order wave effects that result in steady state forces are not accurately captured by the disturbance (subscript 'D') terms. A work-around has been used in this paper to represent these steady state wave effects. To capture this effect, the definition of the wave required a non zero mean for the external flow velocity vector $\boldsymbol{\nu}_{\mathbf{f}}$. A mean of $[0, 0, 0.05, 0, 0, 0]^\top$ was used in this case. This was essentially the same as a very subtle mean current in the vertical plane, which had the effect of biasing the eventual output forces. In a fully featured simulation, this external flow velocity offset would need to be identified as a function of sea state, using either experimental or suitable fidelity numerical simulations.

The results suggest that the predictions of the LNMS model for the forces are slightly greater in magnitude than the measured forces, but within the uncertainty of the experiment. Likewise the moment is slightly under predicted, but also within the experimental uncertainty.

As has been described earlier, a true validation of a model such as this requires data from a free running model in a large manoeuvring basin for validating vehicle response and controlled captive model tests to verify individual force contributions. Nonetheless, the authors contend that the towing tank results presented herein provide sufficient corroboration to show that the identified model is fit for purpose for demonstrating the application of the LNMS.

We again note that only a subset of the LNMS model has been identified. Incorporating the mass matrix $\mathbf{M}_{\mathcal{S}0}$ and associated terms would further increase the model's expressive power. Nonetheless, the results that have been presented corroborate sufficiently well to simulate a wave disturbance.

After building confidence in the model through comparison with lab data, a 6DOF maneuvering model was identified to facilitate the primary objective of this effort: control design. This included ShipMo3D runs for a range of operating conditions relevant to the simulations in this paper, and CFD runs for capturing additional hydrodynamic effects that need to be modeled to create a complete 6DOF manoeuvring model. An overview of the identification process is reproduced in Appendix 10.

4 Tracking Autopilot Design with PHS Form

In this section, a control design for forward speed and attitude tracking based on interconnection and damping assignment techniques for Port Hamiltonian Sytems [PHS] (see [29, 42, 43]) is described. Our intent is to expand prior work of the first and third authors [23] in order to demonstrate how a subset of the LNMS model can be exploited for control design. In presenting this, we do not claim to present a fully featured autopilot. Such a task is out of scope for this paper, which has a focus on demonstrating simulation and control with the LNMS model.

We refer interested readers to prior work of the first author for an understanding of how key missing features would be added. In particular, we refer to integral action coupled with anti-windup [20], guidance on curvilinear trajectories [21], and ballast tanks [23].

For this work, we focus exclusively on the fundamentals of the inner loop, and in particular how to leverage the LNMS model for its construction. Whilst such a controller design is limited in its functionality, it will be sufficient to drive the simulated submarine through a realistic simulation, demonstrating the operation of the LNMS model.

The approach to the design will largely follow [23], which applies IDA-PBC to a model of the BB2 submarine in emergency ascent. The IDA-PBC approach is a feedback equivalence problem in which the open-loop "source" dynamics are matched with desired, closed-loop "target" dynamics

	d (m)	$u = 1.0$ m/s	$u = 1.3$ m/s
X_{uu}	$7.466\,00 \times 10^{-1}$	$-2.115\,13 \times 10^{-3}$	$-2.213\,60 \times 10^{-3}$
	$7.966\,00 \times 10^{-1}$	$-1.996\,30 \times 10^{-3}$	$-2.027\,12 \times 10^{-3}$
	$8.466\,00 \times 10^{-1}$	$-1.953\,59 \times 10^{-3}$	$-1.940\,12 \times 10^{-3}$
	$9.466\,00 \times 10^{-1}$	$-1.925\,11 \times 10^{-3}$	$-1.865\,92 \times 10^{-3}$
	1.146 60	$-1.911\,70 \times 10^{-3}$	$-1.832\,87 \times 10^{-3}$
	1.546 60	$-1.902\,12 \times 10^{-3}$	$-1.821\,20 \times 10^{-3}$
	Deep	$-1.894\,20 \times 10^{-3}$	$-1.894\,20 \times 10^{-3}$
Z_{uu}	$7.466\,00 \times 10^{-1}$	$-1.978\,23 \times 10^{-3}$	$-2.108\,61 \times 10^{-3}$
	$7.966\,00 \times 10^{-1}$	$-1.859\,13 \times 10^{-3}$	$-1.921\,49 \times 10^{-3}$
	$8.466\,00 \times 10^{-1}$	$-1.816\,69 \times 10^{-3}$	$-1.834\,81 \times 10^{-3}$
	$9.466\,00 \times 10^{-1}$	$-1.787\,94 \times 10^{-3}$	$-1.760\,28 \times 10^{-3}$
	1.146 60	$-1.774\,25 \times 10^{-3}$	$-1.727\,88 \times 10^{-3}$
	1.546 60	$-1.764\,67 \times 10^{-3}$	$-1.715\,73 \times 10^{-3}$
	Deep	$-1.757\,82 \times 10^{-3}$	$-1.757\,82 \times 10^{-3}$
M_{uu}	$7.466\,00 \times 10^{-1}$	$-1.069\,88 \times 10^{-3}$	$-1.129\,57 \times 10^{-3}$
	$7.966\,00 \times 10^{-1}$	$-1.007\,62 \times 10^{-3}$	$-1.032\,17 \times 10^{-3}$
	$8.466\,00 \times 10^{-1}$	$-9.854\,36 \times 10^{-4}$	$-9.866\,51 \times 10^{-4}$
	$9.466\,00 \times 10^{-1}$	$-9.704\,08 \times 10^{-4}$	$-9.479\,05 \times 10^{-4}$
	1.146 60	$-9.636\,09 \times 10^{-4}$	$-9.305\,44 \times 10^{-4}$
	1.546 60	$-9.586\,00 \times 10^{-4}$	$-9.244\,04 \times 10^{-4}$
	Deep	$-9.543\,06 \times 10^{-4}$	$-9.543\,06 \times 10^{-4}$
	d (m)	$u = 1.6$ m/s	$u = 1.9$ m/s
X_{uu}	$7.466\,00 \times 10^{-1}$	$-2.275\,99 \times 10^{-3}$	$-2.153\,72 \times 10^{-3}$
	$7.966\,00 \times 10^{-1}$	$-2.063\,37 \times 10^{-3}$	$-2.074\,92 \times 10^{-3}$
	$8.466\,00 \times 10^{-1}$	$-1.958\,87 \times 10^{-3}$	$-1.987\,32 \times 10^{-3}$
	$9.466\,00 \times 10^{-1}$	$-1.848\,71 \times 10^{-3}$	$-1.873\,39 \times 10^{-3}$
	1.146 60	$-1.780\,90 \times 10^{-3}$	$-1.774\,72 \times 10^{-3}$
	1.546 60	$-1.760\,69 \times 10^{-3}$	$-1.723\,22 \times 10^{-3}$
	Deep	$-1.894\,20 \times 10^{-3}$	$-1.894\,20 \times 10^{-3}$
Z_{uu}	$7.466\,00 \times 10^{-1}$	$-2.190\,43 \times 10^{-3}$	$-2.081\,59 \times 10^{-3}$
	$7.966\,00 \times 10^{-1}$	$-1.977\,59 \times 10^{-3}$	$-2.002\,71 \times 10^{-3}$
	$8.466\,00 \times 10^{-1}$	$-1.873\,31 \times 10^{-3}$	$-1.915\,11 \times 10^{-3}$
	$9.466\,00 \times 10^{-1}$	$-1.763\,15 \times 10^{-3}$	$-1.801\,34 \times 10^{-3}$
	1.146 60	$-1.695\,23 \times 10^{-3}$	$-1.702\,74 \times 10^{-3}$
	1.546 60	$-1.674\,91 \times 10^{-3}$	$-1.651\,17 \times 10^{-3}$
	Deep	$-1.757\,82 \times 10^{-3}$	$-1.757\,82 \times 10^{-3}$
M_{uu}	$7.466\,00 \times 10^{-1}$	$-1.167\,39 \times 10^{-3}$	$-1.106\,96 \times 10^{-3}$
	$7.966\,00 \times 10^{-1}$	$-1.056\,27 \times 10^{-3}$	$-1.065\,83 \times 10^{-3}$
	$8.466\,00 \times 10^{-1}$	$-1.001\,62 \times 10^{-3}$	$-1.020\,03 \times 10^{-3}$
	$9.466\,00 \times 10^{-1}$	$-9.440\,30 \times 10^{-4}$	$-9.604\,64 \times 10^{-4}$
	1.146 60	$-9.085\,27 \times 10^{-4}$	$9.089\,22 \times 10^{-4}$
	1.546 60	$-8.980\,44 \times 10^{-4}$	$-8.819\,62 \times 10^{-4}$
	Deep	$-9.543\,06 \times 10^{-4}$	$-9.543\,06 \times 10^{-4}$

Table 2: Results from straight and level CFD simulations for various depths and speeds. Predictions of the total flow model matched CFD results to six significant figures in all conditions

to obtain the feedback control law. The target dynamics in this case must be representable in Port-Hamiltonian form. The source dynamics is likewise modelled in a similar manner to the Port Hamiltonian definition. However, in this case some of the constraints around the definition of a PHS (such as those that guarantee stability) are relaxed.

An input-state-output *Port-Hamiltonian system* (PHS) has the following form (see [44]):

$$\dot{\mathbf{x}} = \left(\check{\mathbf{J}}(\mathbf{x}) - \check{\mathbf{R}}(\mathbf{x})\right) \frac{\partial \mathcal{H}(\mathbf{x})}{\partial \mathbf{x}} + \check{\mathbf{G}}(\mathbf{x})\,\mathbf{u}, \tag{22}$$

$$\mathbf{x} \triangleq \begin{bmatrix} \mathbf{x}_1 \\ \mathbf{x}_2 \end{bmatrix} = \begin{bmatrix} \mathbf{M}\boldsymbol{\nu} \\ \boldsymbol{\eta} \end{bmatrix} \tag{23}$$

$$\mathbf{y} = \check{\mathbf{G}}^{\top}(\mathbf{x}) \frac{\partial \mathcal{H}(\mathbf{x})}{\partial \mathbf{x}}, \tag{24}$$

where $\mathbf{x} \in \mathbb{R}^n$ is the state vector and $\mathcal{H} : \mathbb{R}^n \to \mathbb{R}$ is known as the Hamiltonian. In many cases of engineering interest, the Hamiltonian represents the total energy stored in the system. In the case of this study, the Hamiltonian will represent a sum of energies: kinetic and potential energy of the boat, as well as energy due to its interaction with the fluid and the free surface. The pair $\mathbf{u}, \mathbf{y} \in \mathbb{R}^m$ are the input and output variables. These are conjugate variables – their inner product represents the power exchanged between the system and the environment. The matrix $\check{\mathbf{J}}(\mathbf{x})$ is skew-symmetric and describes the power conserving interconnection structure through which the components of the system exchange energy. The matrix $\check{\mathbf{R}}(\mathbf{x}) \geq 0$ is symmetric and captures dissipative phenomena in the system. The matrix $\check{\mathbf{G}}(\mathbf{x})$ weighs the action of the input on the system and defines the output. From (22) and (24), it follows that

$$\frac{d\mathcal{H}}{dt} = \mathbf{y}^{\top}\mathbf{u} - \frac{\partial \mathcal{H}^{\top}(\mathbf{x})}{\partial \mathbf{x}} \check{\mathbf{R}}(\mathbf{x}) \frac{\partial \mathcal{H}(\mathbf{x})}{\partial \mathbf{x}} \leq \mathbf{y}^{\top}\mathbf{u}, \tag{25}$$

which exhibits the passivity of the PHS model (see [28]).

As with the first author's previous work [20], a key characteristic of the way we apply IDA-PBC to the design, is that the action of sway on the other degrees of freedom is decoupled, effectively suppressing the action of the unactuated dynamics on the actuated dynamics.

As part of this process, the decoupled dynamics is essentially rendered internal and assumed stable. Since the feedback from the decoupled dynamics to the controlled dynamics is broken, we rely on our understanding of the stability properties of the boat (as discussed in [20]) to assert that this internal dynamics is not destabilized by the action of the control law presented in this section. Once the influence of this decoupled dynamics is removed, we delete this state from the state equations and ignore it for the purpose of the stability analysis.

4.1 Dynamic Model in PHS Form

The starting point for the control design work is a representation of the equations of motion in Hamiltonian form. Realisation of the model in this form is facilitated by the fact that the LNMS model was developed as a Lagrangian dynamical systems model. Development of this model was originally motivated in part by the assumption that the Lagrangian representation could be converted to Hamiltonian form by means of the transformation of Legendre [45]. Unfortunately, for the full LNMS model we were not able to derive a compact Hamiltonian representation.

Fortunately, with strategic simplifications, a Hamiltonian with intuitive appeal that is applicable to a control design objective was found. The controller will have no knowledge of the wave field,

which is essentially a disturbance. With these assumptions, it can be shown by elaboration with the transformation of Legendre that the LNMS can then be represented with a valid Hamiltonian with energy variables $\mathbf{x}_1 = \mathbf{M}_T\boldsymbol{\nu} + \mathbf{g}(t)$ and $\mathbf{x}_2 = \boldsymbol{\eta}$, where $\mathbf{M}_T$ is a generalized inertia matrix and $\mathbf{g}(t)$ is related to the Cummins integral.

To implement the control law using these energy variables, we would have had to implement an additional change of coordinates in the control law in order to keep the definition of the target dynamics consistent with our prior work. Moreover, to keep the control law time invariant, we would have to use a technique such as that presented in [46], significantly complicating an already large and complex control law.

Instead, we chose to truncate the source and target dynamics with a further simplification, removing the memory effects integral from the equations. With this simplification, we can use energy variables compatible with prior work, i.e., $\mathbf{x}_1 = \mathbf{M}_T\boldsymbol{\nu}$ and $\mathbf{x}_2 = \boldsymbol{\nu}$. We then proceed with the representation of the source dynamics in Port Hamiltonian form.

This simplification (i.e., the removal of the memory effects integral) is only performed for the model used to synthesise the control law (i.e., both the "source" and "target" dynamics of the PHS). We do not make this simplification in the simulation. The simulated dynamics includes all memory effects, and the simulation bears out that the control design is sufficiently robust to cope despite the modelling uncertainty used in the synthesis of the control law.

To put (1) and (2) into PHS form, we initially follow [19], then augment the equations to incorporate the terms from the LNMS model. In the sequel, we adopt the underscript "p" to denote elements associated with the plant (i.e., source) dynamics used within the control law. Similarly, we will adopt an underscript "c" to denote elements associated with the control-transformed (i.e., target) dynamics. For the χ terms, which represent control forces, we distinguish between the forces generated directly by the control law (c superscript) and control disturbance expressed only on unactuated coordinates (e superscript). These terms are described in section 4.3

$$\underset{\mathrm{p}}{\mathbf{x}} \triangleq \begin{bmatrix} \underset{\mathrm{p}1}{\mathbf{x}} \\ \underset{\mathrm{p}2}{\mathbf{x}} \end{bmatrix} = \begin{bmatrix} \underset{\mathrm{p}}{\mathbf{M}}\left(\underset{\mathrm{p}1}{\mathbf{x}}, \underset{\mathrm{p}2}{\mathbf{x}}\right)\boldsymbol{\nu} \\ \boldsymbol{\eta} \end{bmatrix} \tag{26}$$

$$\dot{\underset{\mathrm{p}}{\mathbf{x}}} = \left(\begin{bmatrix} -\underset{\mathrm{p}}{\mathbf{C}}(\underset{\mathrm{p}1}{\mathbf{x}}, \underset{\mathrm{p}2}{\mathbf{x}}) & -\underset{\mathrm{p}}{\mathbf{J}}^{\top}(\underset{\mathrm{p}2}{\mathbf{x}}) \\ \underset{\mathrm{p}}{\mathbf{J}}(\underset{\mathrm{p}2}{\mathbf{x}}) & \mathbf{0} \end{bmatrix} - \begin{bmatrix} \underset{\mathrm{p}}{\mathbf{D}}(\underset{\mathrm{p}1}{\mathbf{x}}, \underset{\mathrm{p}2}{\mathbf{x}}) & \mathbf{0} \\ \mathbf{0} & \mathbf{0} \end{bmatrix} \right) \frac{\partial \mathcal{H}}{\partial \underset{\mathrm{p}}{\mathbf{x}}} + \begin{bmatrix} \mathbf{I} \\ \mathbf{0} \end{bmatrix} \underset{\mathrm{p}}{\boldsymbol{\chi}}, \tag{27}$$

$$\underset{\mathrm{p}}{\boldsymbol{\chi}} = \overset{\mathrm{c}}{\underset{\mathrm{p}}{\boldsymbol{\chi}}} + \overset{\mathrm{e}}{\underset{\mathrm{p}}{\boldsymbol{\chi}}}, \tag{28}$$

$$\overset{\mathrm{c}}{\underset{\mathrm{p}}{\boldsymbol{\chi}}} = \underset{\mathrm{p}}{\mathbf{B}}(\underset{\mathrm{p}}{\mathbf{x}}, \boldsymbol{\delta}), \tag{29}$$

where

$$\underset{\mathrm{p}}{\mathbf{M}}\left(\underset{\mathrm{p}1}{\mathbf{x}}, \underset{\mathrm{p}2}{\mathbf{x}}\right) \triangleq \mathbf{M}(\boldsymbol{\nu}, \underset{\mathrm{p}2}{\mathbf{x}}, t)|_{t\to\infty} \tag{30}$$

$$\underset{\mathrm{p}}{\mathbf{C}}(\underset{\mathrm{p}1}{\mathbf{x}}, \underset{\mathrm{p}2}{\mathbf{x}}) \triangleq \mathbf{L}_V(\underset{\mathrm{p}}{\mathbf{M}}^{-1}\underset{\mathrm{p}1}{\mathbf{x}}, \underset{\mathrm{p}2}{\mathbf{x}}) + \mathbf{C}(\underset{\mathrm{p}}{\mathbf{M}}^{-1}\underset{\mathrm{p}1}{\mathbf{x}}, \underset{\mathrm{p}2}{\mathbf{x}}, t)|_{t\to\infty}, \tag{31}$$

$$\underset{\mathrm{p}}{\mathbf{J}}(\underset{\mathrm{p}2}{\mathbf{x}}) \triangleq \mathbf{J}(\underset{\mathrm{p}2}{\mathbf{x}}), \qquad \underset{\mathrm{p}}{\mathbf{D}}(\underset{\mathrm{p}1}{\mathbf{x}}, \underset{\mathrm{p}2}{\mathbf{x}}) \triangleq \mathbf{D}(\mathbf{M}^{-1}\underset{\mathrm{p}1}{\mathbf{x}}, \underset{\mathrm{p}2}{\mathbf{x}}, t)|_{t\to\infty}, \qquad \underset{\mathrm{p}}{\mathbf{B}}(\underset{\mathrm{p}1}{\mathbf{x}}) \triangleq \mathbf{B}(\underset{\mathrm{p}}{\mathbf{M}}^{-1}\underset{\mathrm{p}1}{\mathbf{x}}) \tag{32}$$

In the definitions (30) to (32), all external flow and disturbance terms are assumed zero, as the control law has no knowledge of the wave or other disturbances. Furthermore, the matrices from the LNMS model are calculated at infinite time, meaning that the matrices defining the source dynamics will not be time dependent. In this design, we rely on the robustness of the closed loop to compensate for these omissions in the definition of the source dynamics.

The matrix $\underset{\mathrm{p}}{\mathbf{C}}(\underset{\mathrm{p}1}{\mathbf{x}}, \underset{\mathrm{p}2}{\mathbf{x}})$ incorporates all the off-diagonal terms of $\mathbf{H}$, given in (8). These terms (which primarily consist of Coriolis and lift effects) will not satisfy all requirements for the open-loop system to be a PHS because the skew symmetry property of the connectivity structure will not be satisfied. The control law can, however, be designed so that this is corrected in the target (closed-loop) dynamics, so the closed-loop system satisfies all the conditions for a PHS with the desired characteristics.

The Hamiltonian function for the dynamics (33) is the sum of the rigid body and fluid kinetic energy and a potential energy function that accounts for the effect of gravity and buoyancy.

$$\mathcal{H}(\underset{\mathrm{p}}{\mathbf{x}}) = \mathcal{T}(\underset{\mathrm{p}1}{\mathbf{x}}) + \mathcal{V}(\underset{\mathrm{p}2}{\mathbf{x}}) = \frac{1}{2}\,\underset{\mathrm{p}1}{\mathbf{x}}^{\top}\,\underset{\mathrm{p}}{\mathbf{M}}\left(\underset{\mathrm{p}1}{\mathbf{x}}, \underset{\mathrm{p}2}{\mathbf{x}}\right)^{-1}\underset{\mathrm{p}1}{\mathbf{x}} + \mathcal{V}(\underset{\mathrm{p}2}{\mathbf{x}}). \tag{33}$$

To find a suitable potential energy function, the following constraint is imposed on the form of the Hamiltonian (and specifically the potential energy function $\mathcal{V}$):

$$\underset{\mathrm{p}}{\mathbf{J}}^{\top}(\underset{\mathrm{p}2}{\mathbf{x}})\,\frac{\partial \mathcal{H}}{\partial \underset{\mathrm{p}2}{\mathbf{x}}} = \mathbf{g}(\underset{\mathrm{p}2}{\mathbf{x}}) \tag{34}$$

Referring to (7), note that (34) implies

$$\frac{\partial \mathcal{H}}{\partial \underset{\mathrm{p}2}{\mathbf{x}}} = \begin{bmatrix} \mathbf{e}_3\,(b - mg) \\ mg\mathbf{p}^b_{G/O} - b\mathbf{p}^b_{B/O} \\ 0 \end{bmatrix} \tag{35}$$

A useful simplification is to assume that the centre of buoyancy $\mathbf{p}^b_{B/O} = [x_B, y_B, z_B]^{\top}$ coincides with $\mathbf{O}$. This simplifies the potential function considerably, however this simplification is not necessary if the formulation for the potential defined herein is used. The corresponding potential function $\mathcal{V}$ is obtained by integration:

$$\mathcal{V}(\underset{\mathrm{p}2}{\mathbf{x}}) = (b - gm)\,z + gm\mathbf{\Gamma}^{\top}\mathbf{p}^b_{G/O} - b\mathbf{\Gamma}^{\top}\mathbf{p}^b_{B/O} \tag{36}$$

4.2 Velocity and Attitude Tracking

The autopilot will track speed in the actuated velocity coordinates (u,w) as well as the orientation of the vehicle. The target dynamics corresponding to this control action will be realized after a transformation of coordinates from $\underset{\mathrm{p}}{\mathbf{x}}$ to $\underset{\mathrm{c}}{\mathbf{x}}$ that reflects a modified measure of the system energy associated with the target dynamics.

The control will be realised via a force and torque vector, denoted $\underset{\mathbf{p}}{\overset{\mathbf{c}}{\boldsymbol{\chi}}}$, where the overscript "c" stands for "control." This term is one of the two components of the external force $\underset{\mathbf{p}}{\boldsymbol{\chi}}$; the other represents environmental disturbances. The control term $\underset{\mathbf{p}}{\overset{\mathbf{c}}{\boldsymbol{\chi}}}$ comprises two components, in turn: $\underset{\mathbf{p}}{\overset{\mathbf{c}}{\boldsymbol{\chi}}} = \underset{\mathbf{p}}{\overset{\mathbf{t}}{\boldsymbol{\chi}}} - \underset{\mathbf{p}}{\overset{\mathbf{r}}{\boldsymbol{\chi}}}$. The first of these two terms represents a tracking control law. The second is a corrective (or "remediative") control term that accounts for the lack of actuation in sway. The implementation of the force and moment command $\underset{\mathbf{p}}{\overset{\mathbf{c}}{\boldsymbol{\chi}}}$ is achieved using a control allocation strategy.

To design the tracking control law, a process is followed similar to that described in [47], with some extensions to accommodate the fact that the vehicle is underactuated. The control objective is to minimize the tracking error $\underset{\mathrm{c}}{\tilde{\mathbf{x}}}$.

All underwater vehicles will experience a sway force when turning or under the influence of a current with a lateral component. This vehicle has no specific actuation to regulate the sway force, however it is possible to regulate the yaw angle. Since the system is underactuated, the controller is designed such that the sway forces will have no influence on the target dynamics. The effect of control inputs on the actuated degrees of freedom, however, will certainly influence the dynamics in the unactuated (sway) degree of freedom. The dynamics of the actuated degrees of freedom will, however, have an influence over the uncontrolled dynamics. It is assumed that the open-loop stability properties and the closed-loop control design yield stable dynamics in the uncontrolled degrees of freedom, an assumption that is verified after the fact.

To ensure that the uncontrolled dynamics do not affect the dynamics being controlled, the target dynamics is defined so that the uncontrolled sway velocity v has no influence on the controlled states. To achieve this, the desired Coriolis matrix is first chosen to be independent of v, and then the target mass matrix is defined with no off-diagonal terms. That is, the proposed desired Coriolis-centripetal matrix is

$$\underset{c}{\mathbf{C}}(\underset{c1}{\mathbf{x}}) = \begin{bmatrix} 0 & 0 & 0 & mrz_G & m(w-qx_G) & -mrx_G \\ 0 & 0 & 0 & 0 & 0 & 0 \\ 0 & 0 & 0 & -mpz_G & -m(u+qz_G) & mpx_G \\ -mrz_G & 0 & mpz_G & 0 & -pI_{xz}-qI_{yz}+rIzz & pI_{xy}-qI_{yy}+rI_{yz} \\ m(qx_G-w) & 0 & m(u+qz_G) & pI_{xz}+qI_{yz}-rI_{zz} & 0 & pI_{xx}-qI_{xy}-rI_{xz} \\ mrx_G & 0 & -mpx_G & -pI_{xy}+qI_{yy}-rI_{yz} & -pI_{xx}+qI_{xy}+rI_{xz} & 0 \end{bmatrix} \tag{37}$$

In order for the target dynamics to be a PHS, the mass matrix should be positive definite and diagonal.[8] This condition ensures the PHS form (and, consequently, passivity and stability). Moreover, it also ensures that effects due to velocities from other states do not couple onto the unactuated state due to off-diagonal terms. Finally, this form of the target mass matrix also facilitates the synthesis of the correcting controller, which will also be presented later in this paper. For this design, the desired mass matrix $\underset{c}{\mathbf{M}}$ of the target dynamics is a constant diagonal matrix built with the entries of the main diagonal of the original mass matrix $\underset{p}{\mathbf{M}}\left(\underset{p1}{\mathbf{x}}, \underset{p2}{\mathbf{x}}\right)$ corresponding to the deeply submerged state.

Since part of the state ($\underset{p1}{\mathbf{x}}$) is defined in terms of the vehicle mass matrix $\underset{p}{\mathbf{M}}$, a change of coordinates is necessary in order to realise this new mass matrix $\underset{c}{\mathbf{M}}$ in the target dynamics.

A new set of coordinates $\underset{c}{\mathbf{x}}$ is therefore given by

$$\underset{c1}{\mathbf{x}} = \underset{c}{\mathbf{M}}\underset{p}{\mathbf{M}}\left(\underset{p1}{\mathbf{x}}, \underset{p2}{\mathbf{x}}\right)^{-1} \underset{p1}{\mathbf{x}} = \underset{c}{\mathbf{M}}\boldsymbol{\nu}, \tag{38}$$

$$\underset{c2}{\mathbf{x}} = \underset{p2}{\mathbf{x}} \tag{39}$$

Note that each component of the momentum $\underset{c1}{\mathbf{x}}$ is proportional to a corresponding velocity component in $\boldsymbol{\nu}$ since $\underset{c}{\mathbf{M}}$ is diagonal. A tracking error vector, denoted with an over tilde, is defined as the difference between the actual value and a reference value: $\underset{c}{\tilde{\mathbf{x}}} = \underset{c}{\mathbf{x}} - \underset{c}{\mathbf{x}}^*$, where $\underset{c}{\mathbf{x}}^*$ is the new reference trajectory, which is related to $\underset{p}{\mathbf{x}}^*$ as follows:

$$\underset{c}{\mathbf{x}}^*_{\mathbf{1}} = \underset{c}{\mathbf{M}}\underset{p}{\mathbf{M}}\left(\underset{p1}{\mathbf{x}}, \underset{p2}{\mathbf{x}}\right)^{-1} \underset{p}{\mathbf{x}}^*_{\mathbf{1}}, \tag{40}$$

$$\underset{c}{\mathbf{x}}^*_{\mathbf{2}} = \underset{p}{\mathbf{x}}^*_{\mathbf{2}} \tag{41}$$

[8] The PHS form does not mandate a diagonal mass matrix, but for this design it is required.

In the sequel, all of the functions of the desired PHS are specified in terms of the new coordinates $\underset{c}{\mathbf{x}}$. The damping matrix is selected to be symmetric, positive definite, and with the elements proportional to the square of the forward momentum $\underset{c}{x}_u$, which is the first component of $\underset{c}{x}$. Namely,

$$\underset{c}{\mathbf{D}}(\underset{c}{\mathbf{x}}_1) = \text{diag}\left(\left[d_1\underset{c}{x}_u^2 + k_{d_1}, d_2\underset{c}{x}_u^2 + k_{d_2}, d_3\underset{c}{x}_u^2 + k_{d_3}, d_4\underset{c}{x}_u^2 + k_{d_4}, d_5\underset{c}{x}_u^2 + k_{d_5}, d_6\underset{c}{x}_u^2 + k_{d_6}\right]\right) \tag{42}$$

The parameters d_i and k_i with $i \in \{1, \ldots, 6\}$ are positive scalars. The desired Hamiltonian $\underset{c}{\mathcal{H}}(\underset{c}{\tilde{\mathbf{x}}})$ represents the desired system energy of the controlled system. It is designed such that the minimum energy occurs when the tracking error is zero. The gradient of the desired Hamiltonian can be expressed as follows:

$$\frac{\partial \underset{c}{\mathcal{H}}}{\partial \underset{c}{\tilde{\mathbf{x}}}} = \begin{bmatrix} \underset{c}{\mathbf{M}}^{-1}\underset{c}{\tilde{\mathbf{x}}}_1 \\ \text{diag}\left([K_u, 0, K_w]\right)\underset{c}{\tilde{\mathbf{x}}}_{2a} \\ \text{diag}\left([K_{\Gamma 1}, K_{\Gamma 2}, K_{\Gamma 3}]\right)\underset{c}{\tilde{\mathbf{x}}}_{2b} \\ \begin{bmatrix} K_\psi \end{bmatrix}\underset{c}{\tilde{\mathbf{x}}}_{2c} \end{bmatrix}, \tag{43}$$

where

$$\underset{c}{\tilde{\boldsymbol{x}}}_1 = \left[\underset{c}{\tilde{x}}_u, \underset{c}{\tilde{x}}_v, \underset{c}{\tilde{x}}_w, \underset{c}{\tilde{x}}_p, \underset{c}{\tilde{x}}_q, \underset{c}{\tilde{x}}_r\right]^\top \qquad \underset{c}{\tilde{\boldsymbol{x}}}_{2a} = \left[\underset{c}{\tilde{x}}_x, \underset{c}{\tilde{x}}_y, \underset{c}{\tilde{x}}_z\right]^\top \tag{44}$$

$$\underset{c}{\tilde{\boldsymbol{x}}}_{2b} = \left[\underset{c}{\tilde{x}}_{\Gamma 1}, \underset{c}{\tilde{x}}_{\Gamma 2}, \underset{c}{\tilde{x}}_{\Gamma 3}\right]^\top \qquad \underset{c}{\tilde{\boldsymbol{x}}}_{2c} = \left[\underset{c}{\tilde{x}}_\psi\right] \tag{45}$$

The matrix $\underset{c}{\mathbf{J}}$ is chosen to satisfy the constraint

$$\underset{c}{\mathbf{J}}\left(\underset{c}{\tilde{\mathbf{x}}}_2 + \underset{c}{\mathbf{x}_2}^*\right) \triangleq \underset{p}{\mathbf{J}}\left(\underset{c}{\mathbf{x}}_2\right)\Big|_{\underset{c}{\mathbf{x}}_2 = \left(\underset{c}{\tilde{\mathbf{x}}}_2 + \underset{c}{\mathbf{x}_2}^*\right)} \tag{46}$$

The target PHS is therefore defined as follows:

$$\dot{\underset{c}{\tilde{\mathbf{x}}}} = \left(\begin{bmatrix} -\underset{c}{\mathbf{C}}\left(\underset{c}{\tilde{\mathbf{x}}}_1 + \underset{c}{\mathbf{x}_1}^*\right) & -\underset{c}{\mathbf{J}}\left(\underset{c}{\tilde{\mathbf{x}}}_2 + \underset{c}{\mathbf{x}_2}^*\right)^\top \\ \underset{c}{\mathbf{J}}\left(\underset{c}{\tilde{\mathbf{x}}}_2 + \underset{c}{\mathbf{x}_2}^*\right) & 0 \end{bmatrix} - \begin{bmatrix} \underset{c}{\mathbf{D}}\left(\underset{c}{\tilde{\mathbf{x}}}_1, \underset{c}{\mathbf{x}_1}^*\right) & 0 \\ 0 & 0 \end{bmatrix}\right)\frac{\partial \underset{c}{\mathcal{H}}}{\partial \underset{c}{\tilde{\mathbf{x}}}} \tag{47}$$

The IDA method (see [29]) is then applied and a matching equation is solved in order to derive a control law through which the target dynamics (47) is realised. The force vector (expressed in the $\underset{p}{\mathbf{x}}$ coordinates) corresponding to this tracking control law is denoted $\overset{t}{\underset{p}{\chi}}$. It is obtained by matching the original dynamics and the desired dynamics. This is achieved in three steps as follows:

1. The derivative of the tracking error in coordinates $\underset{c}{\mathbf{x}}$ is taken with respect to time

$$\dot{\underset{c}{\tilde{\mathbf{x}}}} = \dot{\underset{c}{\mathbf{x}}} - \dot{\underset{c}{\mathbf{x}}}^* = \begin{bmatrix} \underset{c}{\mathbf{M}}\underset{p}{\mathbf{M}}\left(\underset{p}{\mathbf{x}}_1, \underset{p}{\mathbf{x}}_2\right)^{-1}\left(\dot{\underset{p}{\mathbf{x}}}_1 - \dot{\underset{p}{\mathbf{x}}}_1^*\right) \\ \dot{\underset{p}{\mathbf{x}}}_2 - \dot{\underset{p}{\mathbf{x}}}_2^* \end{bmatrix} \tag{48}$$

2. $\dot{\underset{c}{\tilde{\mathbf{x}}}}$ and $\dot{\underset{p}{\mathbf{x}}}$ in (48) are replaced by the target dynamics (47) and the original dynamics (27), respectively. The source and target dynamics must be expressed in different coordinates, since the target mass matrix is different than the mass matrix of the source dynamics. This difference must be accounted for in the control law, which is presented below in equation (53). To proceed, the definition of the source dynamics in equation (26) is used to define the tracking error, separating the equation into $\dot{\underset{p}{\mathbf{x}}}_1$ and $\dot{\underset{p}{\mathbf{x}}}_2$ elements.

$$\dot{\mathbf{x}}_{\mathrm{p}1} - \dot{\mathbf{x}}^*_{\mathrm{p}1} = \left(-\mathbf{C}_{\mathrm{p}}\left(\mathbf{x}_{\mathrm{p}1}, \mathbf{x}_{\mathrm{p}2}\right) - \mathbf{D}_{\mathrm{p}}\left(\mathbf{x}_{\mathrm{p}1}, \mathbf{x}_{\mathrm{p}2}\right)\right) \frac{\partial \mathcal{H}_{\mathrm{p}}}{\partial \mathbf{x}_{\mathrm{p}1}} - \mathbf{J}_{\mathrm{p}}^{\top}\left(\mathbf{x}_{\mathrm{p}2}\right) \frac{\partial \mathcal{H}_{\mathrm{p}}}{\partial \mathbf{x}_{\mathrm{p}2}} + \overset{\mathbf{t}}{\boldsymbol{\chi}}_{\mathbf{p}} - \dot{\mathbf{x}}^*_{\mathrm{p}_1}, \tag{49}$$
$$\dot{\mathbf{x}}_{\mathrm{p}2} - \dot{\mathbf{x}}^*_{\mathrm{p}2} = \mathbf{J}_{\mathrm{p}}\left(\tilde{\mathbf{x}}_{\mathrm{c}2}, \mathbf{x}_{\mathrm{p}2}\right) \frac{\partial \mathcal{H}_{\mathrm{p}}}{\partial \tilde{\mathbf{x}}_{\mathrm{p}1}} - \dot{\mathbf{x}}^*_{\mathrm{p}2},$$

Likewise, equation (47) is split into its $\tilde{\mathbf{x}}_{\mathrm{c}1}$ and $\tilde{\mathbf{x}}_{\mathrm{c}2}$ components.

$$\tilde{\mathbf{x}}_{\mathrm{c}1} = \left(-\mathbf{C}_{\mathrm{c}}(\tilde{\mathbf{x}}_{\mathrm{c}1} + \mathbf{x}^*_{\mathrm{c}1}) - \mathbf{D}_{\mathrm{c}}\left(\tilde{\mathbf{x}}_{\mathrm{c}1}, \mathbf{x}^*_{\mathrm{c}1}\right)\right) \frac{\partial \mathcal{H}_{\mathrm{c}}}{\partial \tilde{\mathbf{x}}_{\mathrm{c}1}} - \mathbf{J}_{\mathrm{c}}\left(\tilde{\mathbf{x}}_{\mathrm{c}2} + \mathbf{x}^*_{\mathrm{c}2}\right)^{\top} \frac{\partial \mathcal{H}_{\mathrm{c}}}{\partial \tilde{\mathbf{x}}_{\mathrm{c}2}}, \tag{50}$$
$$\dot{\tilde{\mathbf{x}}}_{\mathrm{c}2} = \mathbf{J}_{\mathrm{c}}\left(\tilde{\mathbf{x}}_{\mathrm{c}2} + \mathbf{x}^*_{\mathrm{c}2}\right) \frac{\partial \mathcal{H}_{\mathrm{c}}}{\partial \tilde{\mathbf{x}}_{\mathrm{c}1}}$$

To derive the control law, the source (49) and target dynamics (50) are matched, yielding the following

$$\mathbf{M}_{\mathrm{p}}\left(\mathbf{x}_{\mathrm{p}1}, \mathbf{x}_{\mathrm{p}2}\right) \mathbf{M}_{\mathrm{c}}^{-1} \dot{\tilde{\mathbf{x}}}_{\mathrm{c}1} = (\dot{\mathbf{x}}_{\mathrm{p}1} - \dot{\mathbf{x}}^*_{\mathrm{p}1}) = \left(-\mathbf{C}_{\mathrm{p}}(\mathbf{x}_{\mathrm{p}1}, \mathbf{x}_{\mathrm{p}2}) - \mathbf{D}_{\mathrm{p}}(\mathbf{x}_{\mathrm{p}1}, \mathbf{x}_{\mathrm{p}2})\right) \frac{\partial \mathcal{H}_{\mathrm{p}}}{\partial \mathbf{x}_{\mathrm{p}1}} - \mathbf{J}_{\mathrm{p}}^{\top}(\mathbf{x}_{\mathrm{p}2}) \frac{\partial \mathcal{H}_{\mathrm{p}}}{\partial \mathbf{x}_{\mathrm{p}2}} + \overset{\mathbf{t}}{\boldsymbol{\chi}}_{\mathbf{p}} - \dot{\mathbf{x}}^*_{\mathrm{p}1}, \tag{51}$$

$$\dot{\tilde{\mathbf{x}}}_{\mathrm{c}2} = \dot{\mathbf{x}}_{\mathrm{c}2} - \dot{\mathbf{x}}^*_{\mathrm{c}2}. \tag{52}$$

3. Then, equation (51) is solved for the force vector $\overset{\mathbf{t}}{\boldsymbol{\chi}}_{\mathbf{p}}$, which gives

$$\begin{aligned} \overset{\mathbf{t}}{\boldsymbol{\chi}}_{\mathbf{p}} = & \mathbf{M}_{\mathrm{p}}\left(\mathbf{x}_{\mathrm{p}1}, \mathbf{x}_{\mathrm{p}2}\right) \mathbf{M}_{\mathrm{c}}^{-1} \left(\left(-\mathbf{C}_{\mathrm{c}}\left(\tilde{\mathbf{x}}_{\mathrm{c}1} + \mathbf{x}^*_{\mathrm{c}1}\right) - \mathbf{D}_{\mathrm{c}}\left(\mathbf{x}_{\mathrm{c}1}, \mathbf{x}^*_{\mathrm{c}1}\right)\right) \frac{\partial \mathcal{H}_{\mathrm{c}}}{\partial \tilde{\mathbf{x}}_{\mathrm{c}1}} - \mathbf{J}_{\mathrm{c}}\left(\tilde{\mathbf{x}}_{\mathrm{c}2} + \mathbf{x}^*_{\mathrm{c}2}\right)^{\top} \frac{\partial \mathcal{H}_{\mathrm{c}}}{\partial \tilde{\mathbf{x}}_{\mathrm{c}2}}\right) \\ & - \left(\left(-\mathbf{C}_{\mathrm{p}}\left(\mathbf{x}_{\mathrm{p}1}, \mathbf{x}_{\mathrm{p}2}\right) - \mathbf{D}_{\mathrm{p}}\left(\mathbf{x}_{\mathrm{p}1}, \mathbf{x}_{\mathrm{p}2}\right)\right) \frac{\partial \mathcal{H}_{\mathrm{p}}}{\partial \mathbf{x}_{\mathrm{p}1}} - \mathbf{J}_{\mathrm{p}}^{\top}(\mathbf{x}_{\mathrm{p}2}) \frac{\partial \mathcal{H}_{\mathrm{p}}}{\partial \mathbf{x}_{\mathrm{p}2}} - \dot{\mathbf{x}}^*_{\mathrm{p}\,1}\right) \end{aligned} \tag{53}$$

In addition, the matching equation (52) imposes a constraint in the reference signals - see [47]. From the matching equation the condition $\dot{\tilde{\mathbf{x}}}_{\mathrm{c}2} = \dot{\mathbf{x}}_{\mathrm{c}2} - \dot{\mathbf{x}}^*_{\mathrm{c}2}$ is evident. Noting that $\mathbf{x}_{\mathrm{c}2} = \mathbf{x}_{\mathrm{p}2}$ and replacing the derivative of the states by the state equations it follows that the matching equation is satisfied for

$$\dot{\mathbf{x}}^*_{\mathrm{p}2} = \dot{\mathbf{x}}^*_{\mathrm{c}2} = \mathbf{J}_{\mathrm{p}}\left(\mathbf{x}_{\mathrm{p}}\right) \mathbf{M}_{\mathrm{p}}\left(\mathbf{x}_{\mathrm{p}1}, \mathbf{x}_{\mathrm{p}2}\right)^{-1} \mathbf{x}_{\mathrm{p}1} + \mathbf{J}_{\mathrm{p}}\left(\mathbf{x}_{\mathrm{p}2}\right) \mathbf{M}_{\mathrm{p}}\left(\mathbf{x}_{\mathrm{p}1}, \mathbf{x}_{\mathrm{p}2}\right)^{-1} \mathbf{x}^*_{\mathrm{p}1} \tag{54}$$

In this case, the usable elements in the reference vector $\dot{\mathbf{x}}^*_{\mathrm{c}}$ are the desired speed in the surge and heave directions and the orientation of the submarine. Since the boat is unactuated in the sway direction, the references relating to sway motion are set so as to assure the value of $\mathbf{x}_{\mathbf{v}}{}^*_{\mathrm{p}} = 0$. The remaining reference vector elements are computed to satisfy (54).

4.3 The Correcting Controller

For the tracking controller presented in (53), the target dynamics in the $\mathbf{x}_{\mathrm{c}}$ coordinates (40,41) will have completely decoupled the unactuated coordinates from the actuated coordinates. A problem is however evident when the control action is expressed in the original coordinates $\mathbf{x}_{\mathrm{p}}$.

Since $\underset{\mathrm{p}}{\mathbf{M}} \neq \underset{\mathrm{c}}{\mathbf{M}}$, when the control action $\underset{\mathbf{c}}{\overset{\mathbf{t}}{\boldsymbol{\chi}}}$ is expressed in the $\underset{\mathrm{p}}{\mathbf{x}}$ coordinates, the control vector will include components in unactuated degree of freedom, i.e.,

$$[\underset{\mathrm{p}}{\overset{\mathrm{t}}{\chi}}_{u}, \underset{\mathrm{p}}{\overset{\mathrm{t}}{\chi}}_{v}, \underset{\mathrm{p}}{\overset{\mathrm{t}}{\chi}}_{w}, \underset{\mathrm{p}}{\overset{\mathrm{t}}{\chi}}_{p}, \underset{\mathrm{p}}{\overset{\mathrm{t}}{\chi}}_{q}, \underset{\mathrm{p}}{\overset{\mathrm{t}}{\chi}}_{r}]^{\top} = \underset{\mathrm{p}}{\mathbf{M}}\underset{\mathrm{c}}{\mathbf{M}}^{-1}[\underset{\mathrm{c}}{\overset{\mathrm{t}}{\chi}}_{u}, 0, \underset{\mathrm{c}}{\overset{\mathrm{t}}{\chi}}_{w}, \underset{\mathrm{c}}{\overset{\mathrm{t}}{\chi}}_{p}, \underset{\mathrm{c}}{\overset{\mathrm{t}}{\chi}}_{q}, \underset{\mathrm{c}}{\overset{\mathrm{t}}{\chi}}_{r}]^{\top} \tag{55}$$

where $\underset{\mathrm{p}}{\overset{\mathrm{t}}{\chi}}_{v} \neq 0$. Since the system is unactuated in sway, it would appear that the control law cannot be implemented. With careful design of the target dynamics, it is possible to ensure the omission of this underactuated command results in only a moderate (and insignificant) disturbance. Indeed, the dissipativity property of the closed loop implies that minor variations in the target dynamics like this will not result in instability. In this case, however, we design an additional control input (for the actuated channels) which drives $\underset{\mathrm{p}}{\overset{\mathrm{t}}{\chi}}_{v}$ to zero, with the residual error representing a disturbance to the (stable) unactuated system dynamics only. This approach allows the perturbed, unactuated dynamics to be decoupled from the remaining dynamics in a way that supports stability analysis of the closed loop system.

A correcting control law $\underset{\mathbf{p}}{\overset{\mathbf{r}}{\boldsymbol{\chi}}} = \left[\underset{\mathrm{p}}{\overset{\mathrm{r}}{\chi}}_{u}, \underset{\mathrm{p}}{\overset{\mathrm{r}}{\chi}}_{v}, \underset{\mathrm{p}}{\overset{\mathrm{r}}{\chi}}_{w}, \underset{\mathrm{p}}{\overset{\mathrm{r}}{\chi}}_{p}, \underset{\mathrm{p}}{\overset{\mathrm{r}}{\chi}}_{q}, \underset{\mathrm{p}}{\overset{\mathrm{r}}{\chi}}_{r}\right]^{\top}$ can be derived from a series of simultaneous equations that represent the constraints on the control vector expressed in the $\underset{\mathrm{p}}{\mathbf{x}}$ and $\underset{\mathrm{c}}{\mathbf{x}}$ coordinates.

The following expansions of various control forces and moments, expressed either in the original source variables or in the transformed target variables, reflect the facts that (i) the control system cannot provide actuation in sway and (ii) the corrective control must therefore eliminate any residual sway control command that arises earlier in the design.

$$\underset{\mathbf{p}}{\overset{\mathbf{c}}{\boldsymbol{\chi}}} = [\underset{\mathrm{p}}{\overset{\mathrm{c}}{\chi}}_{u}, 0, \underset{\mathrm{p}}{\overset{\mathrm{c}}{\chi}}_{w}, \underset{\mathrm{p}}{\overset{\mathrm{c}}{\chi}}_{p}, \underset{\mathrm{p}}{\overset{\mathrm{c}}{\chi}}_{q}, \underset{\mathrm{p}}{\overset{\mathrm{c}}{\chi}}_{r}]^{\top} \qquad \underset{\mathbf{p}}{\overset{\mathbf{t}}{\boldsymbol{\chi}}} = [\underset{\mathrm{p}}{\overset{\mathrm{t}}{\chi}}_{u}, \underset{\mathrm{p}}{\overset{\mathrm{t}}{\chi}}_{v}, \underset{\mathrm{p}}{\overset{\mathrm{t}}{\chi}}_{w}, \underset{\mathrm{p}}{\overset{\mathrm{t}}{\chi}}_{p}, \underset{\mathrm{p}}{\overset{\mathrm{t}}{\chi}}_{q}, \underset{\mathrm{p}}{\overset{\mathrm{t}}{\chi}}_{r}]^{\top}$$
$$\underset{\mathbf{c}}{\overset{\mathbf{t}}{\boldsymbol{\chi}}} = [\underset{\mathrm{c}}{\overset{\mathrm{t}}{\chi}}_{u}, 0, \underset{\mathrm{c}}{\overset{\mathrm{t}}{\chi}}_{w}, \underset{\mathrm{c}}{\overset{\mathrm{t}}{\chi}}_{p}, \underset{\mathrm{c}}{\overset{\mathrm{t}}{\chi}}_{q}, \underset{\mathrm{c}}{\overset{\mathrm{t}}{\chi}}_{r}]^{\top} \qquad \underset{\mathbf{p}}{\overset{\mathbf{r}}{\boldsymbol{\chi}}} = [\underset{\mathrm{p}}{\overset{\mathrm{r}}{\chi}}_{u}, \underset{\mathrm{p}}{\overset{\mathrm{r}}{\chi}}_{v}, \underset{\mathrm{p}}{\overset{\mathrm{r}}{\chi}}_{w}, \underset{\mathrm{p}}{\overset{\mathrm{r}}{\chi}}_{p}, \underset{\mathrm{p}}{\overset{\mathrm{r}}{\chi}}_{q}, \underset{\mathrm{p}}{\overset{\mathrm{r}}{\chi}}_{r}]^{\top}$$

Recalling that the complete control force and moment is $\underset{\mathbf{p}}{\overset{\mathbf{c}}{\boldsymbol{\chi}}} = \underset{\mathbf{p}}{\overset{\mathbf{t}}{\boldsymbol{\chi}}} - \underset{\mathbf{p}}{\overset{\mathbf{r}}{\boldsymbol{\chi}}}$ and noting that $\underset{\mathbf{p}}{\overset{(\cdot)}{\boldsymbol{\chi}}} = \underset{\mathrm{p}}{\mathbf{M}}\underset{\mathrm{c}}{\mathbf{M}}^{-1}\underset{\mathbf{c}}{\overset{(\cdot)}{\boldsymbol{\chi}}}$, we solve the following system for the terms in the corrective control law $\underset{\mathbf{p}}{\overset{\mathbf{r}}{\boldsymbol{\chi}}}$ and for the time-varying disturbance $\underset{\mathrm{c}}{\delta}_{v}$ that is induced by this correction:

$$\underset{\mathbf{p}}{\overset{\mathbf{c}}{\boldsymbol{\chi}}} = [\underset{\mathrm{p}}{\overset{\mathrm{c}}{\chi}}u, 0, \underset{\mathrm{p}}{\overset{\mathrm{c}}{\chi}}w, \underset{\mathrm{p}}{\overset{\mathrm{c}}{\chi}}p, \underset{\mathrm{p}}{\overset{\mathrm{c}}{\chi}}q, \underset{\mathrm{p}}{\overset{\mathrm{c}}{\chi}}r]^{\top} = \underset{\mathrm{p}}{\mathbf{M}}\underset{\mathrm{c}}{\mathbf{M}}^{-1}\underset{\mathbf{c}}{\overset{\mathbf{t}}{\boldsymbol{\chi}}} - \underset{\mathbf{p}}{\overset{\mathbf{r}}{\boldsymbol{\chi}}}, \tag{56}$$
$$[\underset{\mathrm{p}}{\overset{\mathrm{t}}{\chi}}_{u}, \underset{\mathrm{p}}{\overset{\mathrm{t}}{\chi}}_{v}, \underset{\mathrm{p}}{\overset{\mathrm{t}}{\chi}}_{w}, \underset{\mathrm{p}}{\overset{\mathrm{t}}{\chi}}_{p}, \underset{\mathrm{p}}{\overset{\mathrm{t}}{\chi}}_{q}, \underset{\mathrm{p}}{\overset{\mathrm{t}}{\chi}}_{r}]^{\top} = \underset{\mathrm{p}}{\mathbf{M}}\underset{\mathrm{c}}{\mathbf{M}}^{-1}[\underset{\mathrm{c}}{\overset{\mathrm{t}}{\chi}}_{u}, 0, \underset{\mathrm{c}}{\overset{\mathrm{t}}{\chi}}_{w}, \underset{\mathrm{c}}{\overset{\mathrm{t}}{\chi}}_{p}, \underset{\mathrm{c}}{\overset{\mathrm{t}}{\chi}}_{q}, \underset{\mathrm{c}}{\overset{\mathrm{t}}{\chi}}_{r}]^{\top}, \tag{57}$$
$$\underset{\mathrm{c}}{\mathbf{M}}\underset{\mathrm{p}}{\mathbf{M}}^{-1}\left([\underset{\mathrm{p}}{\overset{\mathrm{t}}{\chi}}_{u}, \underset{\mathrm{p}}{\overset{\mathrm{t}}{\chi}}_{v}, \underset{\mathrm{p}}{\overset{\mathrm{t}}{\chi}}_{w}, \underset{\mathrm{p}}{\overset{\mathrm{t}}{\chi}}_{p}, \underset{\mathrm{p}}{\overset{\mathrm{t}}{\chi}}_{q}, \underset{\mathrm{p}}{\overset{\mathrm{t}}{\chi}}_{r}]^{\top} - [\underset{\mathrm{p}}{\overset{\mathrm{r}}{\chi}}_{u}, \underset{\mathrm{p}}{\overset{\mathrm{r}}{\chi}}_{v}, \underset{\mathrm{p}}{\overset{\mathrm{r}}{\chi}}_{w}, \underset{\mathrm{p}}{\overset{\mathrm{r}}{\chi}}_{p}, \underset{\mathrm{p}}{\overset{\mathrm{r}}{\chi}}_{q}, \underset{\mathrm{p}}{\overset{\mathrm{r}}{\chi}}_{r}]^{\top}\right) = [\underset{\mathrm{c}}{\overset{\mathrm{t}}{\chi}}_{u}, \underset{\mathrm{c}}{\delta}_{v}, \underset{\mathrm{c}}{\overset{\mathrm{t}}{\chi}}_{w}, \underset{\mathrm{c}}{\overset{\mathrm{t}}{\chi}}_{p}, \underset{\mathrm{c}}{\overset{\mathrm{t}}{\chi}}_{q}, \underset{\mathrm{c}}{\overset{\mathrm{t}}{\chi}}_{r}]^{\top}. \tag{58}$$

where $\underset{\mathrm{c}}{\delta}_{v}$ is a time varying disturbance induced by the correction on the underactuated channel only. The simultaneous equations (56), (57) and (58) can be solved to derive equations for $\underset{\mathrm{p}}{\overset{\mathrm{r}}{\chi}}_{u}, \underset{\mathrm{p}}{\overset{\mathrm{r}}{\chi}}_{v}, \underset{\mathrm{p}}{\overset{\mathrm{r}}{\chi}}_{w}, \underset{\mathrm{p}}{\overset{\mathrm{r}}{\chi}}_{p}, \underset{\mathrm{p}}{\overset{\mathrm{r}}{\chi}}_{q}, \underset{\mathrm{p}}{\overset{\mathrm{r}}{\chi}}_{r}$. These equations implement some essential constraints. The control action expressed in the plant dynamics cannot actuate on the v channel. Likewise, the action of the correcting control law can only influence the v channel of the target dynamics. The selection of the target mass matrix is critical in facilitating a solution, which is generally possible using a computer algebra system.

We present an example for derivation of this correcting control law for the special case of a symmetric mass matrix in [23]. For the case of an asymmetric mass matrix for the source dynamics, which is the case here, the solution to the simultaneous equations is too lengthy to include herein.

Remark 4.1. *If the correcting controller is not used, and* $\overset{\mathrm{t}}{\underset{\mathrm{p}}{\chi}}_{v}$ *is set to zero, a parasitic disturbance will result on the actuated parts of* $\overset{\mathrm{c}}{\underset{\mathrm{p}}{\chi}}_{v}$*. The use of the correcting controller will ensure that* $\overset{\mathrm{t}}{\underset{\mathrm{p}}{\chi}}_{v}$ *is zero, whilst mapping any resulting disturbance to the unactuated part of* $\overset{\mathrm{t}}{\underset{\mathrm{p}}{\chi}}$*. In this sense, the correcting controller does not eliminate the disturbance; it simply shifts it to a different region of the dynamics. It is assumed that the natural stability of the platform will dissipate the disturbance, something that is revisited and verified following completion of the design. An analytical advantage of the approach described here arises below: by omitting the perturbed, but asymptotically stable sway dynamics, the true PHS error dynamics in the remaining degrees of freedom is obtained.*

With the combination of the tracking control law (53) and correcting function $\overset{\mathrm{r}}{\underset{\mathrm{p}}{\boldsymbol{\chi}}}$, the error dynamics in the target system state variables can be written as the target dynamics with a disturbance $\underset{\mathrm{c}}{\delta}_{v}$ in the uncontrolled coordinate as follows:

$$\dot{\tilde{\mathbf{x}}}_{\mathrm{c}1} = \left(\begin{bmatrix} -\mathbf{C}_{\mathrm{c}}(\tilde{\mathbf{x}}_{\mathrm{c}} + \mathbf{x}^{*}_{\mathrm{c}}) & -\mathbf{J}_{\mathrm{p}}(\tilde{\mathbf{x}}_{\mathrm{c}} + \mathbf{x}^{*}_{\mathrm{c}})^{\top} \end{bmatrix} - \begin{bmatrix} \mathbf{D}_{\mathrm{c}}(\tilde{\mathbf{x}}_{\mathrm{c}}, \mathbf{x}^{*}_{\mathrm{c}}) & 0 \end{bmatrix}\right) \frac{\partial \mathcal{H}_{\mathrm{c}}}{\partial \tilde{\mathbf{x}}_{\mathrm{c}1}} - \begin{bmatrix} 0 & \underset{\mathrm{c}}{\delta}_{v} & 0 & 0 & 0 & 0 \end{bmatrix}^{\top} \tag{59}$$

If the dynamics related to the $\underset{\mathrm{c}}{x}_{v}$ state (i.e., the uncontrolled dynamics[9]) are omitted from (59), the following PHS results:

$$\dot{\tilde{\mathbf{x}}}_{\mathrm{t}} = \left(\begin{bmatrix} -\mathbf{C}_{\mathrm{t}}\left(\tilde{\mathbf{x}}_{\mathrm{t}} + \mathbf{x}^{*}_{\mathrm{t}}\right) & -\mathbf{J}_{\mathrm{t}}\left(\tilde{\mathbf{x}}_{\mathrm{t}} + \mathbf{x}^{*}_{\mathrm{t}}\right)^{\top} \\ \mathbf{J}_{\mathrm{t}}\left(\tilde{\mathbf{x}}_{\mathrm{t}} + \mathbf{x}^{*}_{\mathrm{t}}\right) & 0 \end{bmatrix} - \begin{bmatrix} \mathbf{D}_{\mathrm{t}}\left(\tilde{\mathbf{x}}_{\mathrm{t}}, \mathbf{x}^{*}_{\mathrm{t}}\right) & 0 \\ 0 & 0 \end{bmatrix}\right) \frac{\partial \mathcal{H}_{t}}{\partial \tilde{\mathbf{x}}_{\mathrm{t}}}, \tag{60}$$

where $\mathbf{x}_{\mathrm{t}} = [\underset{t}{x}_{u}, \underset{t}{x}_{w}, \underset{t}{x}_{p}, \underset{t}{x}_{q}, \underset{t}{x}_{r}, \underset{t}{x}_{x}, \underset{t}{x}_{z}, \underset{t}{x}_{\phi}, \underset{t}{x}_{\theta}, \underset{t}{x}_{\psi}]^{\top}$, $\mathbf{C}_{\mathrm{t}}$, $\mathbf{D}_{\mathrm{t}}$, $\mathbf{J}_{\mathrm{t}}$, and $\frac{\partial \mathcal{H}_{t}}{\partial \tilde{\mathbf{x}}_{\mathrm{t}}}$ are similarly truncated so that only the controlled dynamics are represented.

The action of v on the controlled states was canceled, which means that in the controlled coordinates given by the dynamics (60), the closed loop is a PHS, which facilitates stability analysis.

Figure 3 illustrates the signal flow for the control design.

4.4 Control Allocation

The control law is realized through a force vector $\overset{\mathrm{c}}{\underset{\mathrm{p}}{\boldsymbol{\chi}}}$. This force is implemented using force actuators – control surfaces and a propeller. The actuator configuration will determine whether the force vector can be effected by one or more approaches. For example, in the case of four aft mounted planes in an X configuration, roll can be controlled in more than one way. The forces due to the actuators are defined in equation (14). A control allocation is used to map the control force vector demanded by the controller into appropriate actuator commands. This allocation makes use of the hydrodynamic coefficients related to the control surface and propulsion model (14-15) and is implemented via a two step process.

[9]This includes the motion in the direction of the sway force, which is damped by the natural stability of the platform.

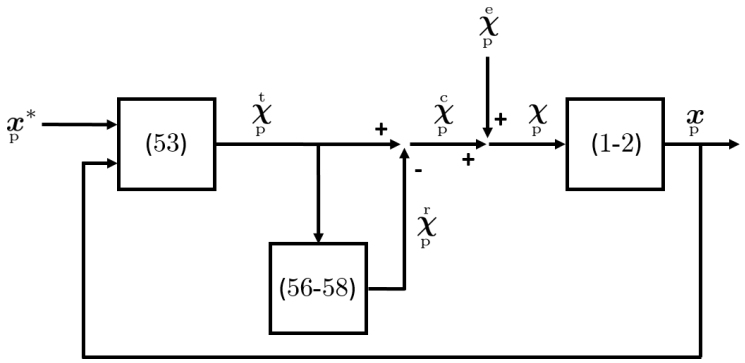

Figure 3: The closed loop control system

First, the allocation to the sail mounted hydroplane and aft control surfaces is determined, based on the desired forces and moments. At this step of the process, which is described in Section 4.4.1, the propeller is not considered, with the exception of the propeller torque K_p, which must be taken into account to ensure that the resulting moments are correct. That is, the aft control surfaces must compensate for the propeller torque, as well as satisfying the demands of the control law.

The result of these calculations is an allocation to a virtual thruster, denoted $A_{\delta T}$, four control surface deflections $A_{\delta X1}$ to $A_{\delta X4}$ and the sail mounted hydroplane $A_{\delta b}$. The allocations resulting from this process form the inputs to the second and final step in the allocation process in which the true propeller RPM command is determined. This step is described in Section 4.4.2.

4.4.1 Control Surfaces

Given that the system is underactuated, and there are different ways to achieve different actuation outcomes, it is necessary to create a function that maps the control forces $\underset{\mathbf{p}}{\overset{\mathbf{c}}{\boldsymbol{\chi}}}$ to the actuator commands $\boldsymbol{\delta}$. This map, denoted $\mathbf{A}\left(\underset{\mathrm{p}}{\mathbf{x}}_1, \underset{\mathrm{p}}{\overset{\mathrm{c}}{\boldsymbol{\chi}}}\right)$ and called the control allocation function, inverts the action of the actuator forces such that the forces commanded by the control law $\underset{\mathbf{p}}{\overset{\mathbf{c}}{\boldsymbol{\chi}}}$ are implemented exactly by the command vector, denoted δ.

In synthesizing a control allocation function, it is useful to consider the symmetries in the actuation hydrodynamics. Given these, the following assumptions can be made

$$
\begin{aligned}
&X_{\delta_{X1}} = X_{\delta_{X2}} = X_{\delta_{X3}} = X_{\delta_{X4}},\\
&Y_{\delta_{X1}} = -Y_{\delta_{X2}},\\
&Y_{\delta_{X3}} = -Y_{\delta_{X4}},\\
&Z_{\delta_{X1}} = Z_{\delta_{X2}} = Z_{\delta_{X3}} = Z_{\delta_{X4}},\\
&K_{\delta_{X1}} = -K_{\delta_{X3}},\\
&K_{\delta_{X2}} = -K_{\delta_{X4}},\\
&K_{\delta_{X3}} = K_{\delta_{X4}},\\
&M_{\delta_{X1}} = M_{\delta_{X2}} = M_{\delta_{X3}} = M_{\delta_{X4}},\\
&N_{\delta_{X1}} = N_{\delta_{X3}},\\
&N_{\delta_{X2}} = -N_{\delta_{X1}},\\
&N_{\delta_{X4}} = N_{\delta X2},\ Y_{\delta_{Xb}} = K_{\delta_{Xb}} = N_{\delta_{Xb}} = 0
\end{aligned}
\tag{61}
$$

Under these assumptions, an allocation matrix was designed based on physical insight into how the control surfaces work in order to achieve the desired force:

$$\underset{\mathrm{p}}{\mathbf{B}}\left(\underset{\mathrm{p}1}{\mathbf{x}}, \mathbf{A}\left(\underset{\mathrm{p}1}{\mathbf{x}}, \overset{\mathrm{c}}{\underset{\mathrm{p}}{\chi}}\right)\right) = \left(\overset{\mathrm{c}}{\underset{\mathrm{p}}{\chi}}u, -\frac{\overset{\mathrm{c}}{\underset{\mathrm{p}}{\chi}}r\, Y_{\delta X2}}{N_{\delta X1}}, \overset{\mathrm{c}}{\underset{\mathrm{p}}{\chi}}w, \overset{\mathrm{c}}{\underset{\mathrm{p}}{\chi}}p, \overset{\mathrm{c}}{\underset{\mathrm{p}}{\chi}}q, \overset{\mathrm{c}}{\underset{\mathrm{p}}{\chi}}r\right)^{\top} \tag{62}$$

For the vehicle under consideration, a solution for the control surface allocation terms of the function $\mathbf{A}\left(\underset{\mathrm{p}1}{\mathbf{x}}, \overset{\mathrm{c}}{\underset{\mathrm{p}}{\chi}}\right)$ is:

$$A_{\delta X1} = -\frac{-K_{\delta X3}\, M_{\delta X1}\, \overset{\mathrm{c}}{\underset{\mathrm{p}}{\chi}}r - K_{\delta X3}\, N_{\delta X1}\, \overset{\mathrm{c}}{\underset{\mathrm{p}}{\chi}}q + M_{\delta X1}\, N_{\delta X1}\, \left(\overset{\mathrm{c}}{\underset{\mathrm{p}}{\chi}}p - K_p\right)}{4K_{\delta X3}\, M_{\delta X1}\, N_{\delta X1}\, u^2} \tag{63}$$

$$\begin{aligned} A_{\delta X2} = {} & \frac{M_{\delta X1}\, N_{\delta X1}\, \left(\overset{\mathrm{c}}{\underset{\mathrm{p}}{\chi}}p - K_p\right) - K_{\delta X3}\, M_{\delta X1}\, \overset{\mathrm{c}}{\underset{\mathrm{p}}{\chi}}r - K_{\delta X3}\, N_{\delta X1}\, \overset{\mathrm{c}}{\underset{\mathrm{p}}{\chi}}q}{4K_{\delta X3}\, M_{\delta X1}\, N_{\delta X1}\, u^2} \\ & - \frac{K_{\delta X3}\, Z_{\delta_b}\, \overset{\mathrm{c}}{\underset{\mathrm{p}}{\chi}}q + M_{\delta_b}\, Z_{\delta X1}\, \left(\overset{\mathrm{c}}{\underset{\mathrm{p}}{\chi}}p - K_p\right) - M_{\delta X1}\, Z_{\delta_b}\, \left(\overset{\mathrm{c}}{\underset{\mathrm{p}}{\chi}}p - K_p\right) - K_{\delta X3}\, M_{\delta_b}\, \overset{\mathrm{c}}{\underset{\mathrm{p}}{\chi}}w}{2K_{\delta X3}\, u^2(M_{\delta_b}\, Z_{\delta X1} - M_{\delta X1}\, Z_{\delta_b})} \end{aligned} \tag{64}$$

$$\begin{aligned} A_{\delta X3} = {} & -\frac{K_{\delta X3}\, Z_{\delta_b}\, \overset{\mathrm{c}}{\underset{\mathrm{p}}{\chi}}q - K_{\delta X3}\, M_{\delta_b}\, \overset{\mathrm{c}}{\underset{\mathrm{p}}{\chi}}w - M_{\delta X1}\, Z_{\delta_b}\, \left(\overset{\mathrm{c}}{\underset{\mathrm{p}}{\chi}}p - K_p\right) + M_{\delta_b}\, Z_{\delta X1}\, \left(\overset{\mathrm{c}}{\underset{\mathrm{p}}{\chi}}p - K_p\right)}{2K_{\delta X3}\, u^2(M_{\delta_b}\, Z_{\delta X1} - M_{\delta X1}\, Z_{\delta_b})} \\ & + \frac{\left(\overset{\mathrm{c}}{\underset{\mathrm{p}}{\chi}}p - K_p\right)\, M_{\delta X1}\, N_{\delta X1} - K_{\delta X3}\, M_{\delta X1}\, \overset{\mathrm{c}}{\underset{\mathrm{p}}{\chi}}r - K_{\delta X3}\, \overset{\mathrm{c}}{\underset{\mathrm{p}}{\chi}}q\, N_{\delta X1}}{4K_{\delta X3}\, M_{\delta X1}\, N_{\delta X1}\, u^2} \end{aligned} \tag{65}$$

$$+ \frac{K_{\delta X3}\, \overset{\mathrm{c}}{\underset{\mathrm{p}}{\chi}}r + N_{\delta X1}\, \left(\overset{\mathrm{c}}{\underset{\mathrm{p}}{\chi}}p - K_p\right)}{2K_{\delta X3}\, N_{\delta X1}\, u^2}$$

$$A_{\delta X4} = \frac{\overset{\mathrm{c}}{\underset{\mathrm{p}}{\chi}}p}{4K_{\delta X3}\, u^2} + \frac{\overset{\mathrm{c}}{\underset{\mathrm{p}}{\chi}}q}{4M_{\delta X1}\, u^2} - \frac{\overset{\mathrm{c}}{\underset{\mathrm{p}}{\chi}}r}{4N_{\delta X1}\, u^2} \tag{66}$$

$$A_{\delta_b} = -\frac{\overset{\mathrm{c}}{\underset{\mathrm{p}}{\chi}}u\, M_{\delta X1} - \overset{\mathrm{c}}{\underset{\mathrm{p}}{\chi}}q\, Z_{\delta X1}}{u^2(M_{\delta_b}\, Z_{\delta X1} - Z_{\delta_b}\, M_{\delta X1})} \tag{67}$$

The process of allocating the control surface values must also determine the actual thrust force required by the propeller. Every deflection results in hydrodynamic drag, which must be countered by the propeller for a perfect control allocation. The allocation function $A_{\delta T}$ (the virtual thruster) determines this value.

$$A_{\delta T} = \overset{\mathrm{c}}{\underset{\mathrm{p}}{\chi}}u - u^2\, X_{\delta_{X1}}\, \delta_{X1}^2 - u^2\, X_{\delta_{X1}}\, \delta_{X2}^2 - u^2\, X_{\delta_{X1}}\, \delta_{X3}^2 - u^2\, X_{\delta_{X1}}\, \delta_{X4}^2 - u^2\, X_{\delta_b}\, \delta_b^2 \tag{68}$$

4.4.2 Propeller RPM

To calculate the desired propeller spin rate, first the desired ratio of advance must be calculated. An equation relating the desired virtual thrust $A_{\delta T}$ to the required advance ratio J_p can be created by solving the standard propeller equations (16-21) for J_p, the result of which is given in (69).

$$J_p = \frac{-D_p^2 K_{t2} \rho u^2 \varrho \pm \sqrt{\kappa}}{2\left(A_{\delta T} + D_p^2 K_{t3} \rho u^2 \varrho\right)}, \tag{69}$$

where

$$\kappa = D_p^4 K_{t2}^2 \rho^2 u^4 \varrho^2 - 4 D_p^2 K_{t1} \rho u^2 \varrho \left(A_{\delta T} + D_p^2 K_{t3} \rho u^2 \varrho \right),$$
$$\varrho = (t_p - 1)(w_t - 1)^2,$$
$$A_{\delta R} = 60 \frac{u - u w_t}{D_p J_p},$$

and $A_{\delta R}$ is the propeller spin rate command, and successively used in the place of $A_{\delta T}$, which is simply the desired thrust force. The procedure for control allocation to the propeller essentially leads to two solutions for κ; i.e., two sets of values for k_t and k_q are available, one set each for the forward and astern quadrants of propeller operation. As a rule, the forward quadrant values are used unless doing so results in a negative κ. Since the propeller equations are quadratic, negative values of κ yield imaginary solutions. A change to a different propeller operation quadrant is therefore required when κ becomes negative.

When operating in the vicinity of the saddle point in the equations, a supervisory algorithm is required to select the correct sign in (69). This can normally be done by selecting the solution closest to the last RPM value, in order to avoid large jumps in the control allocation results.

The propeller dynamics for a platform such as this can be relatively slow compared to the control surfaces. Likewise, no actuator really moves into position at instantaneous speed. For the purposes of this study, the response time for the control surfaces is sufficiently faster than the platform dynamics that they can be neglected. In the case of the propeller, however, this is not necessarily the case. In this study this effect is neglected. More generally, it can be safely ignored if the speed reference u^* generated by the guidance system changes sufficiently slowly for the propulsion control system to keep up.

4.4.3 Combined Allocation

The combined control allocation is assembled as

$$\mathbf{A}\left(\underset{\mathrm{p}}{\mathbf{x}}, \overset{\mathrm{c}}{\underset{\mathrm{p}}{\chi}}\right) = \left(A_{\delta_R}, A_{\delta_{X1}}, A_{\delta_{X2}}, A_{\delta_{X3}}, A_{\delta_{X4}}, A_{\delta_b}\right)^\top. \tag{70}$$

4.5 Tuning

Tuning of the control system was performed following intuition based on the desired system performance, as is frequently done for this kind of control system (see [20]). Tuning was performed for control in all planes by analyzing response to step commands on all axes, initially one at a time, then with combinations of commands.

The objective of the tuning process was to achieve the best compromise between response time, overshoot minimisation and control surface utilisation. The latter consideration was particularly important given that the control surfaces quickly saturate in wave affected conditions. In the tuning process, therefore, it is essential that the control action is not too heavy handed, or the system will saturate too quickly.

This process was continued until the response was deemed satisfactory, such that no improvements could be made against any tuning criteria without negatively affecting the quality of the overall compromise between the objectives. The response of the system to a roll command input was tuned as per the guidance in [20].

The PHS form of the closed loop system guarantees both passivity and stability, meaning that the designer does not need to consider these characteristics during the tuning process. In the first

author's prior work [20], it was demonstrated how integral action can be achieved, and moreover input-to-state stability. With the IDA-PBC control design methodology espoused in the first author's collective work, the structure of the target dynamics itself guarantees the most important characteristics of the closed loop. Tuning is necessary to achieve the final performance characteristics of the closed loop.

5 Stability

The stability of the closed loop is based on its port-Hamiltonian form. Indeed, the Hamiltonian can be chosen as a Lyapunov candidate function and its time derivative along the closed-loop solutions can be computed. (Recall that only the surge, heave and attitude variables are of interest; the stable, but unactuated sway dynamics are omitted.) The time derivative of the Hamiltonian yields

$$\begin{aligned}\frac{d\mathcal{H}_c}{dt} &= \frac{\partial^\top \mathcal{H}_c}{\partial \tilde{\mathbf{x}}_c}\dot{\tilde{\mathbf{x}}}_c = \frac{\partial^\top \mathcal{H}_c}{\partial \tilde{\mathbf{x}}_c}\left[\begin{pmatrix} -\mathbf{C}_c\left(\mathbf{x}_{t1}\right) & -\mathbf{J}_c\left(\mathbf{x}_{t2}\right)^\top \\ \mathbf{J}_c\left(\mathbf{x}_{t1}\right) & 0 \end{pmatrix} - \begin{pmatrix} \mathbf{D}_c\left(\mathbf{x}_{t1}\right) & \mathbf{0} \\ \mathbf{0} & \mathbf{0} \end{pmatrix}\right]\frac{\partial \mathcal{H}_c}{\partial \tilde{\mathbf{x}}_c} \\ &= -\frac{\partial^\top \mathcal{H}_c}{\partial \tilde{\mathbf{x}}_{c1}}\mathbf{D}_c\frac{\partial \mathcal{H}_c}{\partial \tilde{\mathbf{x}}_{c1}} = -\tilde{\mathbf{x}}_{c1}^\top \mathbf{M}_c^{-\top}\mathbf{D}_c\mathbf{M}_c^{-1}\tilde{\mathbf{x}}_{c1} < 0 \end{aligned} \tag{71}$$

Since the matrices $\mathbf{M}_c^{-1}$ and $\mathbf{D}_c$ are symmetric and positive definite, then (71) ensures stability of the origin of the controlled states in $\mathbf{x}_{t1}$. If matching is satisfied (i.e., the condition given by (54) is true), convergence of the tracking error to zero is ensured. This condition is ensured by using a guidance algorithm (see Section 6) that guarantees a suitable command vector is supplied to the tracking control law.

The stability analysis is valid as long as the control allocation strategy is able to effect the forces required to deliver the appropriate tracking response. It is not unusual for control surfaces to be saturated during near surface operation. This proof does not incorporate any consideration of these conditions. We refer the reader, however, to the design in [20], which incorporates integral action, anti-windup and a proof for stability of the closed loop for regulation. The proof used in that work could readily be applied here, once integral action is added. This addition is, however outside the scope of this study.

6 Simulation Results

In this section, simulation results are presented with the control law commanding a scale model of the BB2 submarine. The simulation incorporates all model elements discussed in this paper, including those that are truncated from the model used for control law synthesis, meaning that the simulation is of higher fidelity and represents a very realistic test case.

Identification of the hydrodynamic terms of the model scale BB2 was performed as presented in this paper. All other geometric and inertial parameters used in the simulation are as per [23]. Our personal experience of running the simulations is that the behaviour close to the free surface is extremely rich for a parametric model. The fact that the model captures the interrelationships between manoeuvring forces and free surface effects makes controlling the plant challenging. Using a nonlinear controller in this context has proven to be very effective. The total vehicle response is influenced by: the controller, rigid body dynamics, steady state free surface interaction forces, memory effects (that result in dynamic influences at different frequencies) and the wave effect. There is a richness in the resulting response that is not typical for a parametric model.

Whilst our observation is that the model behaviour is extremely rich, we acknowledge that the model simplifications we performed to facilitate identification would result in some simulation discrepancy. Moreover, we acknowledge that there is scope for significant enhancement of our model of viscous components. Finally, use of a free running model to aid identification would result in a simulation that is both of higher fidelity and more exhaustively validated. For these reasons, it would be very desirable to pursue these tasks in further work.

There are two modalities in manned submarine autopilot design, typically referred to as a "depth keeping" and "depth changing" modes. The autopilot structure presented in this work could in theory be used for both (with suitable parameter selections for the different modes). For this simulation, we choose to simulate a depth keeping case. The reason for this is that depth keeping is very challenging at periscope depth under waves. By demonstrating a depth keeping case, we must perform significant control in the z direction to avoid broaching, and must compensate for both free surface affected trim and the waves.

The control law presented in this work lacks many features typically employed in a fully featured submarine autopilot. Since the controller lacks both integral action and an anti-windup scheme, we have deliberately ensured that the control surfaces only mildly saturate. Nonetheless, with this limitation we have been able to simulate a harsh condition where the boat is quite affected by the various free surface effects. The control law does not completely eliminate sinusoidal motion of the boat, which is useful as we wish to use the simulation to showcase the difference in dynamic loads in response to representative motion.

The scenario shows the system going straight ahead, then turning first to the starboard then to port. The controller holds depth at 0.9466 m during the manoeuvre, with a regular wave at 10 cm amplitude that is from a fixed direction opposing motion of the boat at the start of the simulation.

The simulation shows good tracking of commands, despite the disturbance forces that are present due to the wave disturbances, memory effects and other free surface forces, which vary as a function of state.

Importantly, this simulation demonstrates that the truncation of the LNMS model that was adopted in the definition of the source dynamics of the control law is not really detrimental to performance. Indeed, the passivity of the closed loop means that despite modelling deficiencies in the control law source dynamics, including the removal of both the wave effect terms and the memory effects integral, tracking is still good.

The simulation output is presented in Figures 4 to 6. The results demonstrate that the control law performs as intended, with stable depth keeping during manoeuvres under waves. Figure 4 shows the components of the vessel's linear and angular velocity, resolved in the body-fixed reference frame. Figure 5 shows the vessel's position and attitude during the maneuver. Figure 6 shows the outputs of the control and allocation schemes, that is, the commanded control deflections applied to the vessel's actuators.

In Figure 7, we plot acceleration during simulation in two ways. In the first, we plot the true acceleration. In the second, we show what the acceleration would be if we had used a deeply submerged model. We choose to compare acceleration rather than force to better account for the effect of the added mass. The plots show the considerable difference in apparent acceleration that is realised by the model integrating LNMS.

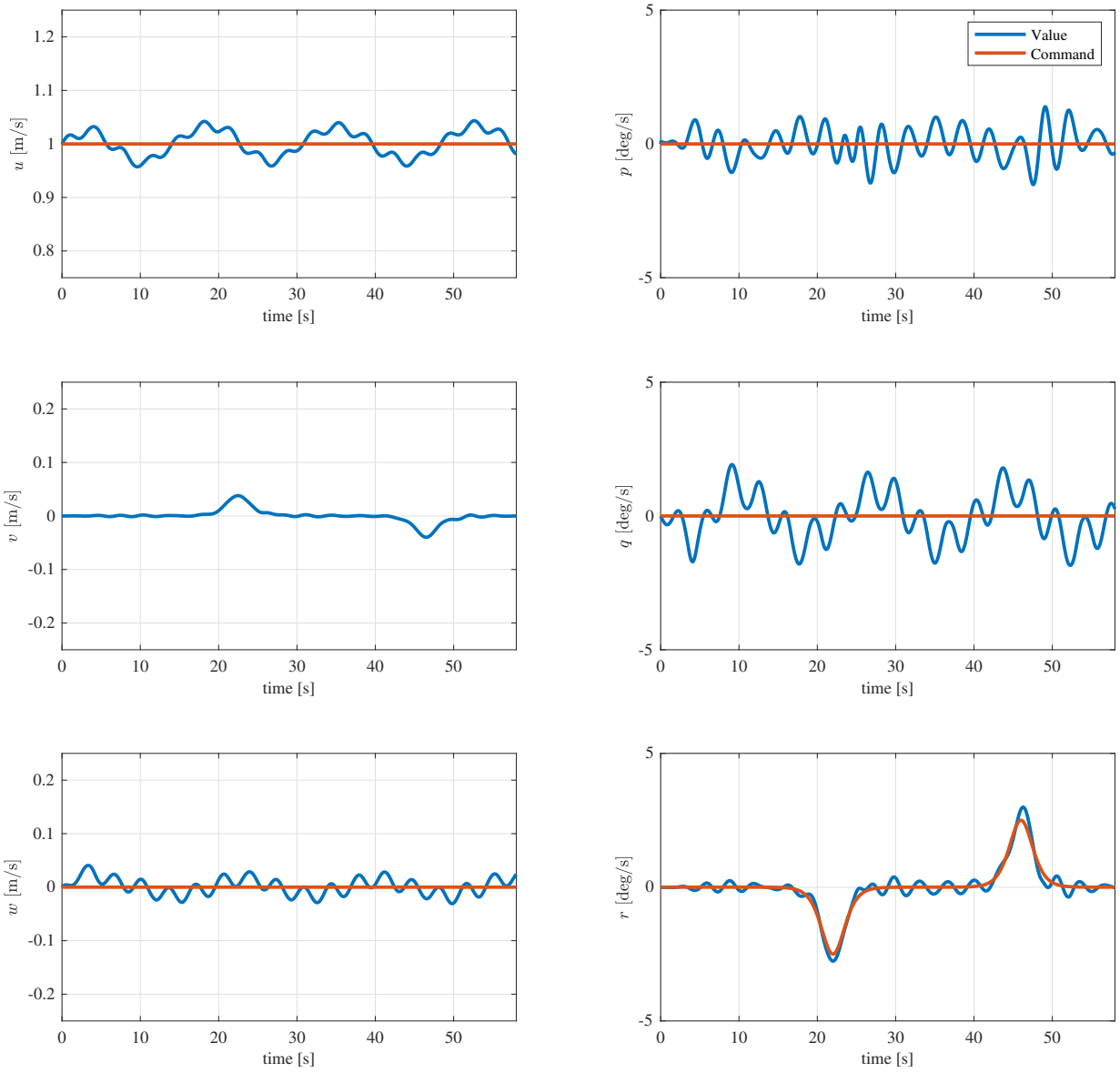

Figure 4: Boat velocity state for the test case

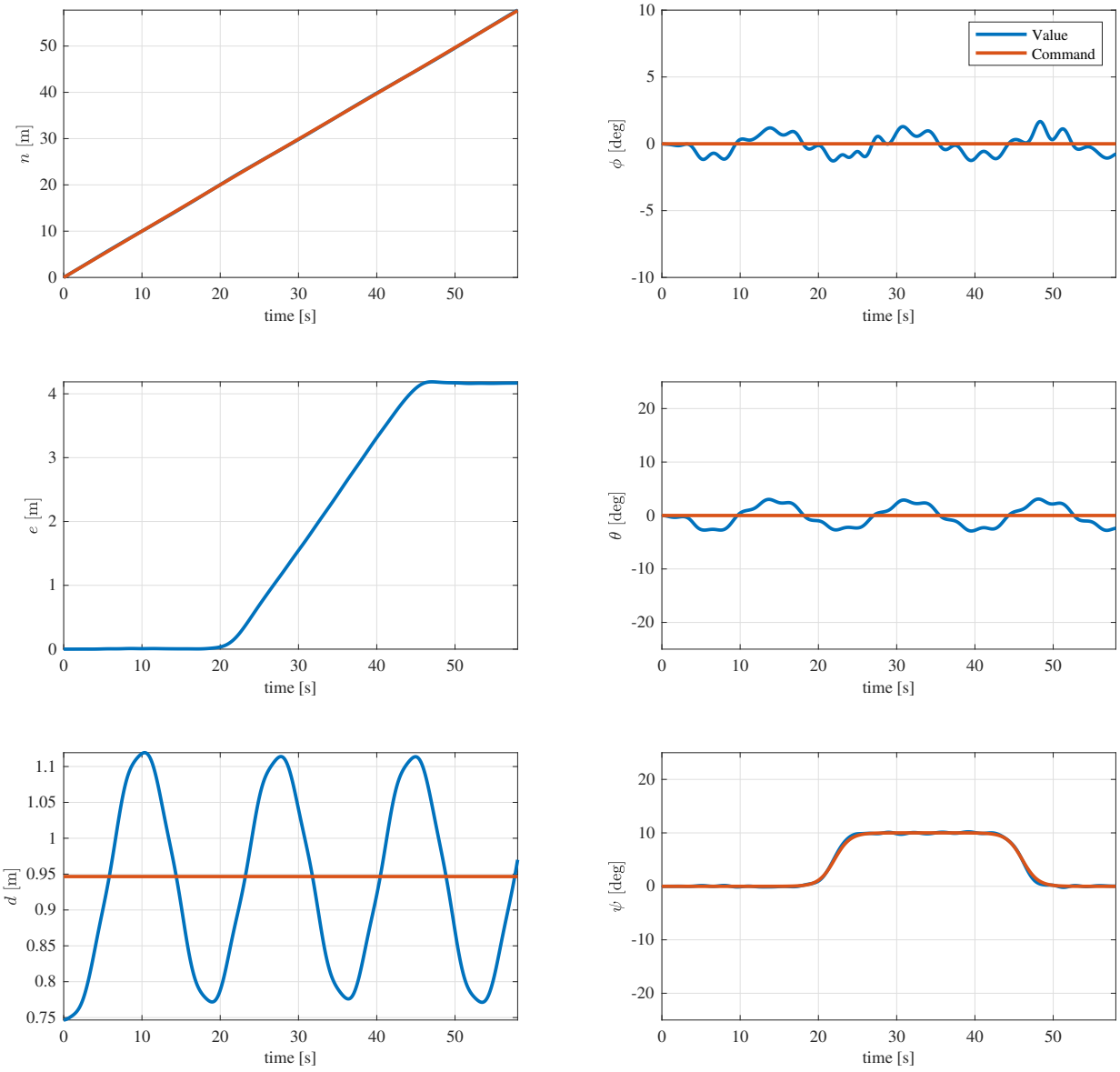

Figure 5: Boat position state for the test case

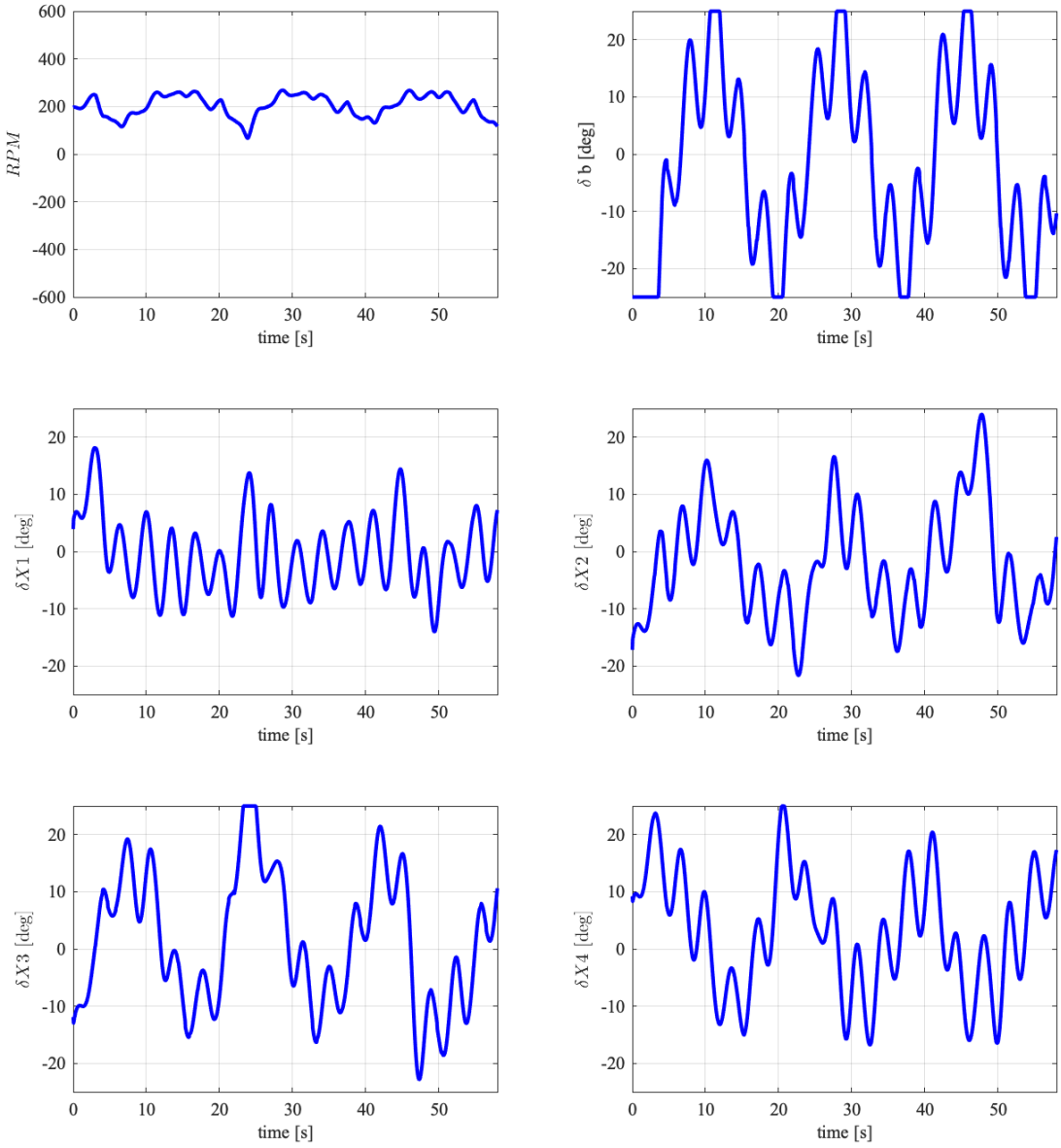

Figure 6: Controller outputs for the test case

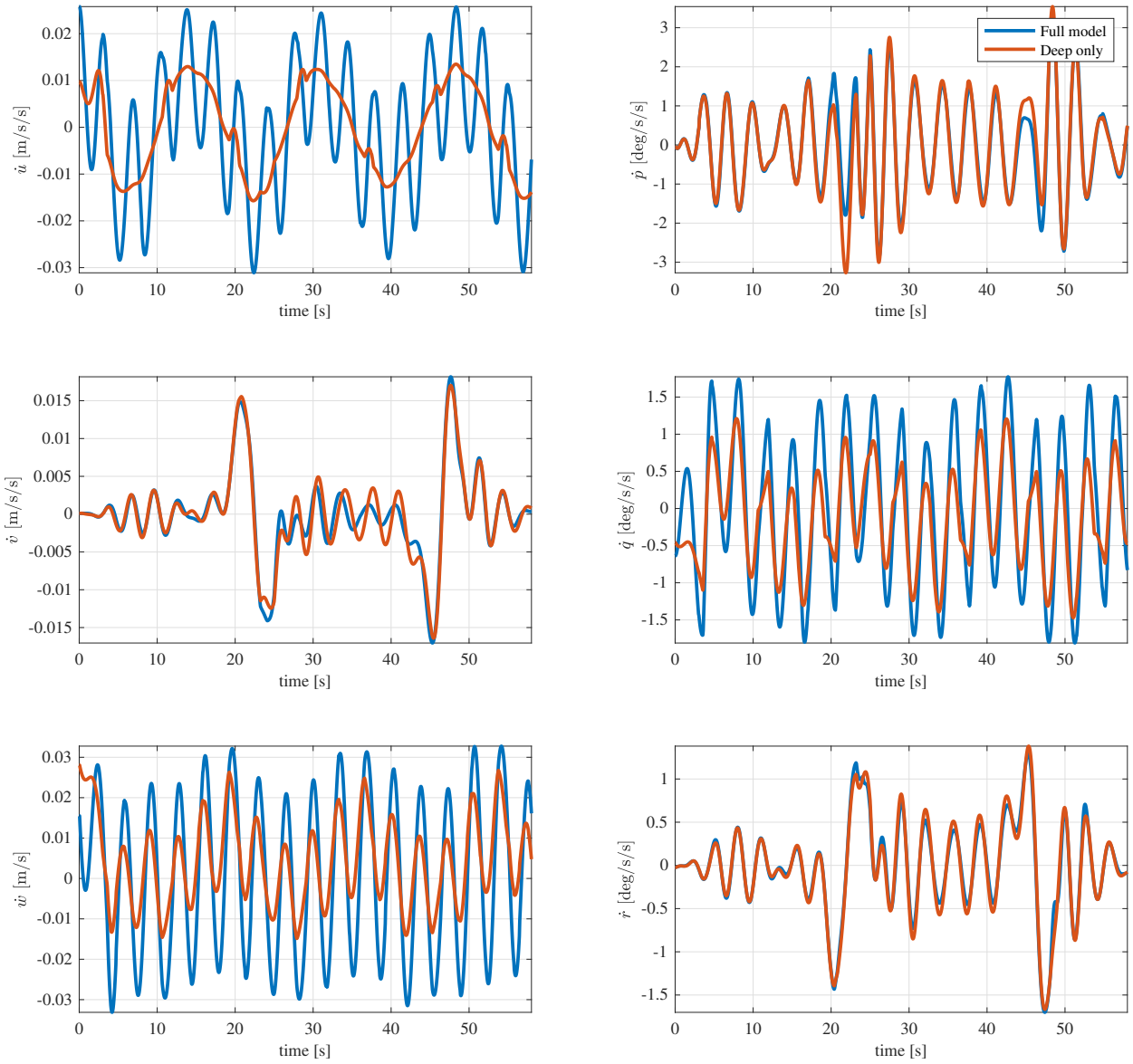

Figure 7: Comparison of the accelerations modeled with the full model vs. a deeply submerged model

7 Discussion & Conclusions

This paper has extended the work of [15, 16, 17], and [23] by demonstrating how to identify, adapt for autopilot design, and simulate the Lagrangian Nonlinear Manoeuvring and Seakeeping (LNMS) unified model. This is the first time the model has been demonstrated for its intended use – model-based control design and stability analysis for a submerged vessel maneuvering in waves. As such, the paper has described significant extensions to prior work. It incorporated the first attempt at identifying a usable subset of the LNMS model using readily available tools. It demonstrated simulation correlation with experimental data acquired in a towing tank. It used a subset of the resulting model as the basis of a nonlinear depth keeping autopilot design. Finally, it presented simulation results for a model scale submarine in a seaway under control of a nonlinear autopilot. This simulation bears out the richness in the simulation capability of the model compared to a traditional model of a deeply submerged submarine. [10]

The depth keeping simulation we present is an interesting test case that showcases the controllers performance in all degrees of freedom. The model presented in this work is identified in all degrees on freedom, and this is necessary for a simulation of depth keeping under waves because in such a scenario the local angle of incidence of the flow to the boat will vary quite a bit in the longitudinal plane, even if the control law manages to keep the boat attitude and depth variation to a minimum.

Despite the fact that only a subset of the model was identified, the output correlated quite well both with straight line CFD simulation results and the wave affected experiment. This result highlights that the terms that were identified are the most significant for prediction of straight and level sailing forces in calm and wave affected conditions. Further work will be required to develop an identification approach that will cover all terms in the model, which we believe will lead to even better correlation in the results.

Comparison with steady state CFD and wave-affected results has given us confidence in the general behaviour of the model. We do not claim, however, that this work represents a complete validation of an identified simulation based on LNMS. This model captures the effects of manoeuvring (angular rates, accelerations) on both the free surface suction effects and wave response. Whilst these effects are simulated in this paper, this behavior has not been validated. Such a validation would either require high fidelity, six degree of freedom (6DOF) driven CFD, or an experiment in a large manoeuvring basin, which was not available to the authors for this work. We defer such activity to future work.

We would like to emphasise here that the simulation behaviour we have observed in this work is very rich specifically for a parametric model. We emphasise this because we are mindful that there are numerous other approaches using geometry based models that also yield very high fidelity simulation results. Noteworthy examples are simulation tools employing on-line execution of time domain panel codes, or indeed 6DOF coupled CFD simulation. Comparison of output with these excellent tools is beyond the scope of this work, for which we focus on evaluating a strictly parametric model. There are advantages of such a model relative to geometry based ones, such as model-based control and estimation, rapid tuning, traceability of control parameters to physical effects, etc. LNMS does not make any assumptions as to whether the simulated boat is in shallow or deep water. The model structure accommodates both, however the mass matrices that need to be identified in LNMS will

[10] Whilst we have not demonstrated it in the present paper, the LNMS model also provides a convenient simulation tool that can be used for other purposes such as the real-time generation of dynamically feasible reference trajectories and analytical nonlinear seakeeping analysis.

have different values in a shallow water condition.We have not made an attempt to demonstrate such functionality here, something we defer to future work.

The wave model presented in this work facilitated simulation of a regular wave, which is demonstrated in the simulation. The design and demonstration of this functionality is an important step toward the objective of demonstrating a model that is capable of representing irregular wave behavior. For full sized submarines, the forces due to frequency difference are significant. It would be possible to perform accurate simulation of irregular waves with a superposition of multiple wave components, however an empirical model would need to be developed to represent the frequency difference influence as a virtual current. The authors believe, however that a better approach would be to extend LNMS to directly support irregular wave modelling. We defer this task to future work.

The autopilot design presented herein satisfies two important objectives. The first is to demonstrate how the LNMS model can be utilised in autopilot design. The second is to develop a control law that can drive a simulation of a model scale submarine so as to demonstrate the behaviour of the LNMS model. It succeeds on both of these counts, but we acknowledge that it is far from a complete autopilot design. In particular, but not exclusively, integral action, anti-windup, guidance, restoring forces compatible with surfaced operation, control of tanks, and signature reduction adjuncts are all critical elements that could be added in future work. Readers are referred the first author's work in this field for an understanding of some of these topics as they relate to the core of the design presented herein [20], [21], [48], [23].

Despite the effectiveness of the control law presented in this work, we make no claims that this design is either optimal or uniquely positioned to benefit from the LNMS model. The work of [23] was conveniently available to us for this activity, and indeed the IDA-PBC control scheme has proven itself to work well. We believe, however, that it would be interesting to see this model applied to the development of other control schemes, both non-linear and indeed linear. The non-linearity of the LNMS model lends itself to adoption within the context of a nonlinear control law. Nonetheless there is no reason why a carefully gain scheduled linear scheme could not benefit from it as well. We defer this to future work and invite others to explore how this model structure could benefit other autopilot design approaches.

There is one additional area that would add value to this work, which is the use of an observer to estimate the sea state. Use of an observer could greatly assist control law performance in wind-wave (as opposed to swell) dominated scenarios.

8 Acknowledgements

We would like to thank Prof. Eric Paterson and Prof. Stefano Brizzolara for their assistance and support in the project. Dr. Tristan Perez first dreamed of unified sea keeping and manoeuvring models in a Lagrangian setting - it is thanks to his encouragement, advice and support that this work was possible. Many people contributed data to system identification efforts. we would like to single out Dr. Gregory Seil, Ms. Mai-Chi Nguyen, and Dr. Alexander Conway for their CFD work, and Mr. Gregory Wright for his work with ShipMo3D. Working with the first author, Dr. Zhi Quan Leong, Dr. Jonathan Duffy and a team of DST contractors and AMC staff made the experiment happen. A license for a beta test version of ShipMo3D was provided by DRDC Canada thanks to the initiative of Dr. Kevin McTaggart. Without all of these people this work would not have been possible. The contribution of the first author was made while he was a member of staff at DST Group, and part of that work was conducted while he was a visiting scholar at Virginia Tech.

The secondment to Virginia Tech was facilitated by the Office of Naval Research (ONR) which also funded the work at Virginia Tech through Grant Nos. N00014-{14-1-0651, 16-1-2749, 20-1-2621}.

References

[1] T. Battista, S. Jung, C. A. Woolsey, and E. G. Paterson, "An energy-Casimir approach to underwater vehicle depth and heading regulation in short crested waves," in *IEEE Conference on Control Technology and Applications (CCTA)*, 2017, pp. 217–222.

[2] E. Liceaga-Castro and G. M. van der Molen, "Submarine h-infinity depth control under wave disturbances," *IEEE Transactions on Control Systems Technology*, vol. 3, no. 3, pp. 338–346, 1995.

[3] J. L. Dantas, J. J. da Cruz, and E. A. de Barros, "Study of autonomous underwater vehicle wave disturbance rejection in the diving plane," *Proceedings of the Institution of Mechanical Engineers, Part M: Journal of Engineering for the Maritime Environment*, vol. 228, no. 2, pp. 122–135, 2014.

[4] L. Moreira and C. G. Soares, "H_2 and H_∞ designs for diving and course control of an autonomous underwater vehicle in presence of waves," *IEEE Journal of Oceanic engineering*, vol. 33, no. 2, pp. 69–88, 2008.

[5] J. S. Riedel, L. Jeffery, S. Riedel, and A. J. Healey, "Model based predictive control of auvs for station keeping in a shallow water wave environment," 1998.

[6] Z. Hong-han, W. Di, L. Cong-cong, and Y. Zhe-ping, "Research on depth control based on output disturbance observer for uuvs maneuvering near the surface," in *2012 IEEE International Conference on Mechatronics and Automation*. IEEE, 2012, pp. 2564–2568.

[7] S. Liu, D. Wang, and E. Poh, "Non-linear output feedback tracking control for auvs in shallow wave disturbance condition," *International Journal of Control*, vol. 81, no. 11, pp. 1806–1823, 2008.

[8] Q. Yang, D.-x. Gao, K. Liang, and J.-j. Hou, "Nonlinear optimal vibration control for auvs with input delay under wave disturbances," in *2019 Chinese Control And Decision Conference (CCDC)*. IEEE, 2019, pp. 5340–5345.

[9] D.-x. Gao, J. Cheng, and Q. Yang, "Depth control for underactuated auv in vertical plane using optimal internal model controller," in *2016 Chinese Control and Decision Conference (CCDC)*. IEEE, 2016, pp. 5292–5296.

[10] Q. Yang, H. Su, J. Zhang, and G.-y. Tang, "Nonlinear optimal internal model control for auvs under wave disturbances," in *2017 29th Chinese Control And Decision Conference (CCDC)*. IEEE, 2017, pp. 2847–2852.

[11] N. Fischer, D. Hughes, P. Walters, E. M. Schwartz, and W. E. Dixon, "Nonlinear rise-based control of an autonomous underwater vehicle," *IEEE Transactions on Robotics*, vol. 30, no. 4, pp. 845–852, 2014.

[12] X. Yao and G. Yang, "Efficient multivariable generalized predictive control for autonomous underwater vehicle in vertical plane," *Mathematical Problems in Engineering*, vol. 2016, 2016.

[13] T. Perez, *Ship motion control: course keeping and roll stabilisation using rudder and fins*. Springer Science & Business Media, 2006.

[14] J. Pinkster, "Low frequency second order wave exciting forces on floating structures," Ph.D. dissertation, 1980.

[15] T. Battista, "Lagrangian mechanics modeling of free surface-affected marine craft," Ph.D. dissertation, Virginia Tech, Blacksburg, VA, May 2018.

[16] T. Battista, F. Valentinis, and C. Woolsey, "A maneuvering model for an underwater vehicle near a free surface—part 1: Motion without memory effects," *IEEE Journal of Oceanic Engineering*, 2018.

[17] ——, "A maneuvering model for an underwater vehicle near a free surface—part 2: Motion with memory effects," *IEEE Journal of Oceanic Engineering*, 2022, (In review.).

[18] C. Woolsey and L. Techy, "Cross-track control of a slender, underactuated auv using potential shaping," *Ocean Engineering*, vol. 36, pp. 82–91, 2009.

[19] A. Donaire and T. Perez, "Dynamic positioning of marine craft using a port-Hamiltonian framework," *Automatica*, vol. 48, no. 5, pp. 851–856, 2012.

[20] F. Valentinis, A. Donaire, and T. Perez, "Energy-based motion control of a slender hull unmanned underwater vehicle," *Ocean Engineering*, vol. 104, pp. 604–616, 2015.

[21] ——, "Energy-based guidance of an underactuated unmanned underwater vehicle on a helical trajectory," *Control Engineering Practice*, vol. 44, pp. 138–156, 2015.

[22] T. Battista, C. Woolsey, L. McCue-Weill, E. Paterson, and F. Valentinis, "Underwater vehicle depth and attitude regulation in plane progressive waves," in *Conference on Decision and Control (CDC)*, 2015.

[23] F. Valentinis and C. Woolsey, "Nonlinear control of a subscale submarine in emergency ascent," *Ocean Engineering*, vol. 171, pp. 646–662, 2019.

[24] M. Gertler and G. Hagen, "Standard equations of motion for submarine simulation," David Taylor Naval Ship Research and Development Center, Tech Report 2510, 1967.

[25] N. E. Leonard, "Stability of a bottom-heavy underwater vehicle," *Automatica*, vol. 33, no. 3, pp. 331 – 346, 1997. [Online]. Available: http://www.sciencedirect.com/science/article/pii/S0005109896001768

[26] J. Marsden and T. Ratiu, *Introduction to Mechanics and Symmetry*. Springer, 1999.

[27] P. G. Thomasson and C. A. Woolsey, "Vehicle motion in currents," *IEEE Journal of Oceanic Engineering*, vol. 38, no. 2, pp. 226–242, 2013.

[28] A. van der Schaft, *L2-Gain and Passivity Techniques in Nonlinear Control*, ser. Communications and Control Engineering. Springer Verlag, London, 2000.

[29] R. Ortega, A. van der Schaft, B. Maschke, and G. Escobar, "Interconnection and damping assignment passivity-based control of port-controlled Hamiltonian systems," *Automatica*, vol. 38, no. 4, pp. 585–596, 2002.

[30] A. Astolfi, D. Chhabra, and R. Ortega, "Asymptotic stabilisation of some equilibria of an underactuated underwater vehicle," *Systems and Control letters*, no. 45, pp. 193–206, 2002.

[31] T. I. Fossen, *Handbook of Marine Craft Hydrodynamics and Motion Control*. Wiley, 2011.

[32] B. Brogliato, R. Lozano, B. Maschke, and O. Egeland, *Dissipative System Analysis and Control*. Springer-Verlag, London, 2007.

[33] D. E. Chang, A. M. Bloch, N. E. Leonard, J. E. Marsden, and C. A. Woolsey, "The equivalence

of controlled lagrangian and controlled hamiltonian systems," *ESAIM: Control, Optimisation and Calculus of Variations*, vol. 8, pp. 393–422, 2002.

[34] A. Donaire and T. Perez, "Port-hamiltonian theory of motion control for marine craft," in *Proceedings of the IFAC Conference on Control Applications in Marine Systems*, Rostock, Germany, 2010.

[35] T. P. Crook, "An initial assessment of free surface effects on submerged bodies," Master's thesis, Naval Postgraduate School, Monterey CA, September 1994.

[36] J. Feldman, "DTNSRDC revised standard submaine equstions of motion," David Taylor Naval Ship Research and Development Center, Tech Report DTNSRDC/SPD-0393-09, 1979.

[37] W. Cummins, "The impulse response function and ship motions," David Taylor Model Basin Washington DC, Tech. Rep., 1962.

[38] S. Y. Jung, "Determining parameters for a Lagrangian mechanical system model of a submerged vessel maneuvering in waves," Ph.D. dissertation, Virginia Tech, 2020.

[39] S. Jung, S. Brizzolara, and C. A. Woolsey, "An approach for computing parameters for a lagrangian nonlinear maneuvering and seakeeping model of submerged vessel motion," *IEEE Journal of Oceanic Engineering*, 2021, dOI:0.1109/JOE.2021.3052657 (To appear.).

[40] A. Conway, F. Valentinis, and G. Seil, "Characterisation of suction effects on a submarine body operating near the free surface," in *21st Australasian fluid mechanics conference, Adelaide, Australia, paper*, vol. 766, 2018.

[41] E. Morelli, "System identification programs for aircraft (SIDPAC)," in *AIAA Atmospheric Flight Mechanics Conference and Exhibit*, 2002, p. 4704.

[42] K. Fujimoto and T. Sugie., "Canonical transformation and stabilization of generalized hamiltonian systems." *Systems and Control Letters*, 2001.

[43] A. Donaire and S. Junco, "On the addition of integral action to port-controlled Hamiltonian systems," *Automatica*, vol. 45, no. 8, pp. 1910–1916, 2009.

[44] A. van der Schaft, "Port-Hamiltonian systems: an introductory survey," in *Proceeding of the International Congress of Mathematicians*, 2006.

[45] V. I. Arnol'd, *Mathematical methods of classical mechanics*. Springer Science & Business Media, 2013, vol. 60.

[46] T. Pérez and T. Fossen, "Time-vs. frequency-domain identification of parametric radiation force models for marine structures at zero speed," *Modeling, Identification and Control*, vol. 29, no. 1, pp. 1–19, 2008.

[47] A. Donaire, J. Romero, and T. Perez, "Trajectory tracking passivity-based control for marine vehicles subject to disturbances," *Journal of the Franklin Institute*, vol. 354, pp. 2167–2182, 2017.

[48] A. Donaire, F. Valentinis, , T. Perez, and J. Ford, "Nonlinear energy shaping and damping injection control of a ship in a seaway, submitted for review," *Journal of Marine Science and Technology*, 2022.

[49] P. Joubert, "Some aspects of submarine design," DEFENCE SCIENCE AND TECHNOLOGY ORGANISATION VICTORIA (AUSTRALIA) PLATFORM SCIENCES LAB, Tech. Rep., 2004.

[50] MARIN, "BB2 Dataset," http://www.marin.nl/web/ships-structures/navy/submarines.htm,

2015.

[51] G. Seil, N. M, D. Pook, and Z. Leong, "CFD study of the hydrodynamics of the evolved DST Group generic submarine (BB2)," Tech. Rep., 2017.

[52] H. J. Bohlmann, "Berechnung hydrodynamischer koeffizienten von ubooten zur vorhersage des bewegungsverhaltens," Ph.D. dissertation, 1990.

[53] K. A. McTaggart, "Verification and validation of ShipMo3D ship motion predictions in the time and frequency domains," *International Journal of Naval Architecture and Ocean Engineering*, vol. 3, no. 1, pp. 86–94, 2011.

9 Explicit Expressions for Hydrodynamic Parameters

The equations of motion generated from the Lagrangian function (11) are [15]:

$$\begin{aligned}\mathbf{0} = &\left(\boldsymbol{M}_{\mathrm{b}} + \boldsymbol{M}_{\mathrm{I}}(\boldsymbol{\eta},\boldsymbol{\nu}) + \boldsymbol{M}_{\mathrm{M}}(\boldsymbol{\eta},\boldsymbol{\nu},t) + \boldsymbol{M}_{\mathrm{E}}(\boldsymbol{\eta},\boldsymbol{\nu},t)\right)\dot{\boldsymbol{\nu}} \\ &+ \left(\boldsymbol{C}_{\mathrm{b}}(\boldsymbol{\nu}) + \boldsymbol{C}_{\mathrm{I}}(\boldsymbol{\eta},\boldsymbol{\nu}) + \boldsymbol{C}_{\mathrm{M}}(\boldsymbol{\eta},\boldsymbol{\nu},t) + \boldsymbol{C}_{\mathrm{E}}(\boldsymbol{\eta},\boldsymbol{\nu},t)\right)\boldsymbol{\nu} \\ &+ \left(\boldsymbol{D}_{\mathrm{I}}(\boldsymbol{\eta},\boldsymbol{\nu}) + \boldsymbol{D}_{\mathrm{M}}(\boldsymbol{\eta},\boldsymbol{\nu},t) + \boldsymbol{D}_{\mathrm{E}}(\boldsymbol{\eta},\boldsymbol{\nu},t)\right)\boldsymbol{\nu} \\ &+ \int_0^t \boldsymbol{K}_{\mathrm{M}}(\boldsymbol{\eta},\boldsymbol{\nu},\boldsymbol{\eta}(\tau),t-\tau)\boldsymbol{\nu}(\tau)d\tau \\ &+ \boldsymbol{M}_{\mathrm{D}}(\boldsymbol{\eta},\boldsymbol{\nu},t)\dot{\boldsymbol{\nu}}_{\mathrm{f}} + \boldsymbol{C}_{\mathrm{D}}(\boldsymbol{\eta},\boldsymbol{\nu},t)\boldsymbol{\nu}_{\mathrm{f}} + \boldsymbol{D}_{\mathrm{D}}(\boldsymbol{\eta},\boldsymbol{\nu},t)\boldsymbol{\nu}_{\mathrm{f}}\end{aligned} \tag{72}$$

The terms $\boldsymbol{M}_{\mathrm{I}}$, $\boldsymbol{C}_{\mathrm{I}}$ and $\boldsymbol{D}_{\mathrm{I}}$ are the "instantaneous" fluid response matrices. These terms account for the energy required to generate the instantaneous fluid response to the motion of a rigid body. Some of these terms will remain for a deeply submerged vehicle. Explicitly,

$$\begin{aligned}\boldsymbol{M}_{\mathrm{I}}(\boldsymbol{\nu},\boldsymbol{\eta}) = &\boldsymbol{M}_{\mathcal{B}} + \Delta\boldsymbol{M}_{\mathcal{B}} + \boldsymbol{M}_{\mathcal{S}_0} \\ &+ \sum_{i=1}^{6}\left((\boldsymbol{e}_i\boldsymbol{\nu}^T)\frac{\partial \boldsymbol{M}_{\mathcal{S}_0}}{\partial \nu_i} + \frac{\partial \boldsymbol{M}_{\mathcal{S}_0}}{\partial \nu_i}(\boldsymbol{\nu}\boldsymbol{e}_i^T)\right) + \frac{1}{2}\sum_{i=1}^{6}\sum_{j=1}^{6}(\boldsymbol{e}_i\boldsymbol{\nu}^T)\frac{\partial^2 \boldsymbol{M}_{\mathcal{S}_0}}{\partial \nu_i \partial \nu_j}(\boldsymbol{\nu}\boldsymbol{e}_j^T)\end{aligned} \tag{73}$$

$$\boldsymbol{C}_{\mathrm{I}}(\boldsymbol{\nu},\boldsymbol{\eta}) = \boldsymbol{G}\left[\boldsymbol{M}_{\mathcal{B}} + \Delta\boldsymbol{M}_{\mathcal{B}} + \boldsymbol{M}_{\mathcal{S}_0} + \frac{1}{2}\sum_{i=1}^{6}(\boldsymbol{e}_i\boldsymbol{\nu}^T)\frac{\partial \boldsymbol{M}_{\mathcal{S}_0}}{\partial \nu_i}\right] \tag{74}$$

$$\begin{aligned}\boldsymbol{D}_{\mathrm{I}}(\boldsymbol{\nu},\boldsymbol{\eta}) = &\sum_{i=1}^{6}\left(\boldsymbol{J}_i^T\boldsymbol{\nu}\mathbb{I} - \frac{1}{2}\boldsymbol{J}_i\boldsymbol{\nu}^T\right)\left(\frac{\partial \Delta\boldsymbol{M}_{\mathcal{B}}}{\partial \eta_i} + \frac{\partial \boldsymbol{M}_{\mathcal{S}_0}}{\partial \eta_i}\right) \\ &+ \frac{1}{2}\sum_{i=1}^{6}\sum_{j=1}^{6}\left(\boldsymbol{J}_j^T\boldsymbol{\nu}\right)\left(\boldsymbol{e}_i\boldsymbol{\nu}^T\right)\frac{\partial^2 \boldsymbol{M}_{\mathcal{S}_0}}{\partial \nu_i \partial \eta_j}\end{aligned} \tag{75}$$

The terms $\boldsymbol{M}_{\mathrm{M}}$, $\boldsymbol{C}_{\mathrm{M}}$, $\boldsymbol{D}_{\mathrm{M}}$, and $\boldsymbol{K}_{\mathrm{M}}$ are the "memory-effect" matrices. These terms account for the cumulative fluid energy which is radiated away from the body in the form of surface waves. These terms vanish for a deeply submerged vehicle. Explicitly,

$$\boldsymbol{M}_{\mathrm{M}}(\boldsymbol{\eta},\boldsymbol{\nu},t) = \int_0^t \left[\sum_{i=1}^{6} \boldsymbol{e}_i\boldsymbol{\nu}^T(\tau)\frac{\partial \boldsymbol{K}_{\mathcal{S}_0}^T(t-\tau)}{\partial \nu_i} + \frac{\partial \boldsymbol{K}_{\mathcal{S}_0}(t-\tau)}{\partial \nu_i}\boldsymbol{\nu}(\tau)\boldsymbol{e}_i^T\right] d\tau$$
$$+ \int_0^t \left[\sum_{i=1}^{6}\sum_{j=1}^{6} \boldsymbol{e}_i\boldsymbol{\nu}^T \frac{\partial^2 \boldsymbol{K}_{\mathcal{S}_0}(t-\tau)}{\partial \nu_i \partial \nu_j}\boldsymbol{\nu}(\tau)\boldsymbol{e}_j^T\right] d\tau \tag{76}$$

$$\boldsymbol{C}_{\mathrm{M}}(\boldsymbol{\eta},\boldsymbol{\nu},t) = \boldsymbol{G}\int_0^t \sum_{i=1}^{6} \boldsymbol{e}_i\boldsymbol{\nu}^T(\tau)\frac{\partial \boldsymbol{K}_{\mathcal{S}_0}^T(t-\tau)}{\partial \nu_i} d\tau$$
$$- \int_0^t \begin{pmatrix} \boldsymbol{0} & \boldsymbol{K}_1(\widehat{t-\tau})\boldsymbol{\nu}(\tau) \\ \boldsymbol{K}_1(\widehat{t-\tau})\boldsymbol{\nu}(\tau) & \boldsymbol{K}_2(\widehat{t-\tau})\boldsymbol{\nu}(\tau) \end{pmatrix} d\tau \tag{77}$$

$$\boldsymbol{D}_{\mathrm{M}}(\boldsymbol{\eta},\boldsymbol{\nu},t) = \int_0^t \sum_{i=1}^{6} \left(\frac{\partial \boldsymbol{K}_{\mathcal{S}_0}(t-\tau)}{\partial q_i}\boldsymbol{\nu}(\tau)\boldsymbol{J}_i^T - \boldsymbol{J}_i\boldsymbol{\nu}(\tau)^T\frac{\partial \boldsymbol{K}_{\mathcal{S}_0}^T(t-\tau)}{\partial q_i}\right) d\tau$$
$$+ \int_0^t \sum_{i=1}^{6}\sum_{j=1}^{6} \boldsymbol{e}_i\boldsymbol{\nu}^T(\tau)\left[(\boldsymbol{J}_j^T\boldsymbol{\nu})\frac{\partial^2 \boldsymbol{K}_{\mathcal{S}_0}^T(t-\tau)}{\partial q_j \partial \nu_i} + \frac{\partial^2 \boldsymbol{K}_{\mathcal{S}_0}^T(t-\tau)}{\partial \nu_i \partial (t-\tau)}\right] d\tau \tag{78}$$

$$\boldsymbol{K}_{\mathrm{M}}(\boldsymbol{\eta},\boldsymbol{\nu},\boldsymbol{\eta}(\tau),t-\tau) = \frac{\partial\left(\boldsymbol{K}_{\mathcal{B}}(\boldsymbol{\eta}(\tau),t-\tau) + \boldsymbol{K}_{\mathcal{S}_0}(\boldsymbol{\eta},\boldsymbol{\nu},\boldsymbol{\eta}(\tau),t-\tau)\right)}{\partial(t-\tau)} \tag{79}$$

and

$$\boldsymbol{K}_1(\boldsymbol{\eta},\boldsymbol{\nu},\boldsymbol{\eta}(\tau),t-\tau) = \begin{pmatrix}\mathbb{I}_{3\times 3} & \boldsymbol{0}_{3\times 3}\end{pmatrix}\left(\boldsymbol{K}_{\mathcal{B}}(\boldsymbol{\eta}(\tau),t-\tau) + \boldsymbol{K}_{\mathcal{S}_0}(\boldsymbol{\nu},\boldsymbol{\eta},\boldsymbol{\eta}(\tau),t-\tau)\right)$$
$$\boldsymbol{K}_2(\boldsymbol{\nu},\boldsymbol{\eta},\boldsymbol{\eta}(\tau),t-\tau) = \begin{pmatrix}\boldsymbol{0}_{3\times 3} & \mathbb{I}_{3\times 3}\end{pmatrix}\left(\boldsymbol{K}_{\mathcal{B}}(\boldsymbol{\eta}(\tau),t-\tau) + \boldsymbol{K}_{\mathcal{S}_0}(\boldsymbol{\nu},\boldsymbol{\eta},\boldsymbol{\eta}(\tau),t-\tau)\right)$$

The terms $\boldsymbol{M}_{\mathrm{E}}$, $\boldsymbol{C}_{\mathrm{E}}$, and $\boldsymbol{D}_{\mathrm{E}}$ are the "external" flow perturbation matrices. These terms account for the modifications to the calm water system energy due to the external flow field. This is the phenomena observed by Crook [35], who measured the changes to the calm-water free surface suction and wave resistance forces due to incident waves. Explicitly,

$$\boldsymbol{M}_{\mathrm{E}}(\boldsymbol{\nu},\boldsymbol{\eta},t) = -\sum_{i=1}^{6}\left(\boldsymbol{e}_i\boldsymbol{\nu}_{\mathrm{f}}^T\frac{\partial \boldsymbol{M}_{\mathcal{S}_0}}{\partial \nu_i} + \frac{\partial \boldsymbol{M}_{\mathcal{S}_0}}{\partial \nu_i}\boldsymbol{\nu}_{\mathrm{f}}^T\boldsymbol{e}_i\right)$$
$$+ \sum_{i=1}^{6}\sum_{j=1}^{6}\left(\boldsymbol{e}_i\boldsymbol{\nu}_{\mathrm{f}}^T\frac{\partial^2 \boldsymbol{M}_{\mathcal{S}_0}}{\partial \nu_i \partial \nu_j}\left(\frac{1}{2}\boldsymbol{\nu}_{\mathrm{f}} - \boldsymbol{\nu}\right)\boldsymbol{e}_j^T\right) \tag{80}$$

$$\boldsymbol{C}_{\mathrm{E}}(\boldsymbol{\nu},\boldsymbol{\eta},t) = -\boldsymbol{G}\sum_{i=1}^{6}\left(\boldsymbol{e}_i\boldsymbol{\nu}_{\mathrm{f}}^T\frac{\partial \boldsymbol{M}_{\mathcal{S}_0}}{\partial \nu_i}\right) \tag{81}$$

$$\boldsymbol{D}_{\mathrm{E}}(\boldsymbol{\nu},\boldsymbol{\eta},t) = -\begin{pmatrix}\boldsymbol{\Phi} & \boldsymbol{0} \\ -\hat{\boldsymbol{v}}_{\mathrm{f}} & \boldsymbol{0}\end{pmatrix}\left(\boldsymbol{M}_{\mathrm{b}} + \boldsymbol{M}_{\mathcal{B}} + \Delta\boldsymbol{M}_{\mathcal{B}} + \boldsymbol{M}_{\mathcal{S}_0}\right) - \sum_{i=1}^{6}\left(\boldsymbol{e}_i\dot{\boldsymbol{\nu}}_{\mathrm{f}}^T\frac{\partial \boldsymbol{M}_{\mathcal{S}_0}}{\partial \nu_i}\right)$$
$$+ \sum_{i=1}^{6}\left(\boldsymbol{J}_i\boldsymbol{\nu}_{\mathrm{f}}^T\frac{\partial(\Delta\boldsymbol{M}_{\mathcal{B}} + \boldsymbol{M}_{\mathcal{S}_0})}{\partial \eta_i} - \frac{\partial(\Delta\boldsymbol{M}_{\mathcal{B}} + \boldsymbol{M}_{\mathcal{S}_0})}{\partial \eta_i}\boldsymbol{\nu}_{\mathrm{f}}\boldsymbol{J}_i^T\right)$$
$$+ \sum_{i=1}^{6}\sum_{j=1}^{6}\left(\boldsymbol{e}_i\boldsymbol{\nu}_{\mathrm{f}}^T\frac{\partial^2 \boldsymbol{M}_{\mathcal{S}_0}}{\partial \nu_i \partial \eta_j}\left(\frac{1}{2}\boldsymbol{\nu}_{\mathrm{f}} - \boldsymbol{\nu}\right)\boldsymbol{J}_j^T\right) \tag{82}$$

The terms $\boldsymbol{M}_{\mathrm{D}}$, $\boldsymbol{C}_{\mathrm{D}}$, and $\boldsymbol{D}_{\mathrm{D}}$ are the wave "disturbance" matrices. These terms would remain if the vehicle were arrested and therefore account for the energy which results in wave excitation forces. Explicitly,

$$\begin{aligned}\boldsymbol{M}_{\mathrm{D}}(\boldsymbol{\nu},\boldsymbol{\eta},t) &= -\boldsymbol{M}_{\mathrm{b}} - \boldsymbol{M}_{\mathcal{B}} - \Delta\boldsymbol{M}_{\mathcal{B}} - \boldsymbol{M}_{\mathcal{S}_0} \\ &\quad + \sum_{i=1}^{6} \boldsymbol{e}_i \boldsymbol{\nu}_{\mathrm{f}}^T \frac{\partial \boldsymbol{M}_{\mathcal{S}_0}}{\partial \nu_i} + \begin{pmatrix} \boldsymbol{0} & \boldsymbol{0} \\ m_{\mathrm{b}}\hat{\boldsymbol{r}}_{\mathrm{cm}} & \boldsymbol{0} \end{pmatrix} \end{aligned} \tag{83}$$

$$\begin{aligned}\boldsymbol{C}_{\mathrm{D}}(\boldsymbol{\nu},\boldsymbol{\eta},t) &= \boldsymbol{G}\left(-\boldsymbol{M}_{\mathrm{b}} - \boldsymbol{M}_{\mathcal{B}} - \Delta\boldsymbol{M}_{\mathcal{B}} - \boldsymbol{M}_{\mathcal{S}_0}\right) \\ &\quad + \boldsymbol{G}\left(\frac{1}{2}\sum_{i=1}^{6} \boldsymbol{e}_i \boldsymbol{\nu}_{\mathrm{f}}^T \frac{\partial \boldsymbol{M}_{\mathcal{S}_0}}{\partial \nu_i} + \begin{pmatrix} \boldsymbol{0} & \boldsymbol{0} \\ m_{\mathrm{b}}\hat{\boldsymbol{r}}_{\mathrm{cm}} & \boldsymbol{0} \end{pmatrix}\right) \end{aligned} \tag{84}$$

$$\begin{aligned}\boldsymbol{D}_{\mathrm{D}}(\boldsymbol{\nu},\boldsymbol{\eta},t) &= \begin{pmatrix} \boldsymbol{\Phi} & \boldsymbol{0} \\ -\hat{\boldsymbol{v}}_{\mathrm{f}} & \boldsymbol{0} \end{pmatrix}\left(\boldsymbol{M}_{\mathrm{b}} + \boldsymbol{M}_{\mathcal{B}} + \Delta\boldsymbol{M}_{\mathcal{B}} + \boldsymbol{M}_{\mathcal{S}_0}\right) \\ &\quad - \frac{1}{2}\sum_{i=1}^{6}\left(\boldsymbol{J}_i \boldsymbol{\nu}_{\mathrm{f}}^T \frac{\partial(\Delta\boldsymbol{M}_{\mathcal{B}} + \boldsymbol{M}_{\mathcal{S}_0})}{\partial \eta_i}\right) \end{aligned} \tag{85}$$

10 Extended Discussion of System Identification Approach

10.1 Identification of the deep submerged hydrodynamics

The deeply submerged hydrodynamics of the model scale BB2 submarine geometry [49], [50] was identified by means of a combination of high fidelity Reynolds-averaged Navier-Stokes (RANS) computational fluid dynamics (CFD) runs, which were used to characterise the velocity dependencies, and Defence Research and Development Canada (DRDC) ShipMo3D panel code runs, which were used to populate the deeply submerged added mass. The resulting deeply submerged parameter set is identical to the model presented by the first and third author in [23].

ANSYS Fluent was used for the CFD. A 60,883,158 cell mesh was developed and tested for mesh sensitivity. Simulations were performed using the Wilcox K-ω-SST turbulence model. Results were benchmarked against high fidelity simulations from other parties working in the Submarine Hydrodynamics Working Group, where good correlation of results was observed. Straight ahead, incidence and rotating arm tests in CFD were used to characterise the deeply submerged coefficients [51].

A panel mesh representing the model scale BB2 was created for the frequency domain sea keeping code DRDC ShipMo3D. Mesh resolution and simulation settings were selected based on experience both within Canadian and Australian defence departments using the code to create submarine simulations. In the case of the panel mesh, the submarine body and main fin were modelled. The panel mesh did not include the aft control surfaces. To account for the influence of the control surfaces, the empirical approach described by Bohlmann [52] was employed for the deep submerged environment.

10.2 Identification of the LNMS model

The identification of the full LNMS model is challenging as the various matrices in the model have numerous terms which are state dependent. In this work, we demonstrate a process to populate a useful subset of the model using readily available tools. The development of this identification

approach, which has not been previously published, predates the work of Jung [38],[39] and uses different analysis codes.

We commence with the same simplifications used by Jung. In this case, it is assumed that the matrix $\mathbf{M}_{\mathcal{S}0}$ is zero, and that likewise the matrix kernel function $\mathbf{K}_{\mathcal{S}0}$ is also zero. This significantly reduces the system identification process of the LNMS model to identification of the matrices $\mathbf{M}_{\mathcal{B}}$, $\Delta\mathbf{M}_{\mathcal{B}}$ and the matrix kernel function $\mathbf{K}_M$.

The results from the simulation and experimentation tasks conducted as part of this work lead us to believe that these simplifying assumptions are reasonable, because there has been no significantly negative impact on the model's ability to represent the potential contributions to either steady state free surface affected forces or indeed wave response.

The starting point for the characterisation of the remaining terms is the use of a frequency domain sea keeping code. The added mass calculated by the sea keeping code can be broken down into the components $\mathbf{M}_{\mathcal{B}} + \Delta\mathbf{M}_{\mathcal{B}}$ where $\mathbf{M}_{\mathcal{B}}$ is the deeply submerged added mass. This leaves $\Delta\mathbf{M}_{\mathcal{B}}$, which is simply the difference between the actual overall added mass as a function of depth, assuming a non-deformable free surface, and the deeply submerged added mass. In this work, we used a lookup table of added mass as a function of depth that was populated using ShipMo3D.

The kernel function $\boldsymbol{K}_{\mathcal{B}}$ is very closely related to the "retardation function" in the Cummins integral [37]. It is essentially a non linear version of the Cummins retardation, with the extension that it is a function of time and the state of the boat in past time. Since most sea keeping codes are able to compute the Cummins retardation, we exploit such a code for this purpose. In this work, the Cummins retardation was computed using the 3D panel code DRDC ShipMo3D version 4 [53].

ShipMo3D provided a good "baseline" identification. At the time of writing, however, ShipMo3D did not reproduce high fidelity free surface suction results. It is intuitive to think of free surface suction only as a velocity dependent effect (which it is). In the LNMS model, however, all model matrices that relate velocity to forces (such as the damping and Coriolis matrices) are functions of added mass matrices. Whilst ShipMo3D generated predictions for all of the added mass terms, where free surface suction was significant the accuracy of these predictions was insufficient for the task at hand. For this reason, CFD simulations of the submarine sailing parallel to the free surface at steady velocity were used to initially fine-tune the ShipMo3D added mass results for three key added mass terms. Following this, towing tank results were further used to refine the identification of these LNMS terms.

The following relations, derived from a simplification of the LNMS model, were therefore useful for establishing initial guesses for some critical parameters for when the boat was sailing straight and level with no incidence angle:

Letting the subscript "pfs" indicate straight and level motion parallel to the free surface, we

have

$$
\begin{aligned}
X|\text{pfs} &= 0, \\
Y|\text{pfs} &= 0, \\
Z|\text{pfs} &= -\frac{1}{2}u^2\frac{\partial \Delta \mathbf{M}_{\mathcal{B}11}}{\partial d}, \\
K|\text{pfs} &= -\frac{1}{2}u^2\frac{\partial \Delta \mathbf{M}_{\mathcal{B}11}}{\partial \phi}, \\
M|\text{pfs} &= -\frac{1}{2}u^2\left(\frac{\partial \Delta \mathbf{M}_{\mathcal{B}11}}{\partial \theta} + 2\Delta \mathbf{M}_{\mathcal{B}13} + 2\Delta \mathbf{M}_{k31}\right), \\
N|\text{pfs} &= -\frac{1}{2}u^2\left(\mathbf{M}_{k21} - 2\frac{\partial \mathbf{M}_{\mathcal{B}11}}{\partial d}\right)
\end{aligned} \tag{86}
$$

The matrix $\mathbf{M}_k = \mathbf{M}_b + \mathbf{M}_{\mathcal{B}}$ is the total deeply submerged added mass. Using (86), the terms $\mathbf{M}_{\mathcal{B}11}$, $\mathbf{M}_{\mathcal{B}13}$ and their gradients with respect to depth can be approximated as a function of depth using the non-viscous component of the force deduced from a CFD simulation. This is an initial approximation only, because the non-viscous contribution is not the same as the potential flow contribution, as it incorporates effects due to simulated flow being rotational.

In order to identify the terms in (86), the steady RANS CFD simulation described in [51] was modified and extended by addition of the free surface. A time dependent simulation of the submarine sailing at a constant speed parallel to the free surface was developed from that baseline. In order to reduce the heavy computational overhead of time dependent simulations incorporating the free surface, a simplified port side half mesh was adopted. The resulting grid consisted of fully structured hexahedral cells utilising an O-C topology around the hull and appendages with an H topology to create a refinement layer for the free surface. After the various simplifications, the resulting mesh was significantly smaller than the original, at approximately 10 million cells. The overall approach to the simulation, which is described in [40], was validated by benchmarking the results against experimental data from experiments jointly conducted by DST group and the Australian Maritime College (AMC).

Figure 8 shows a visualisation of one of the runs. The visualisation shows that the most important flow structures caused by the free surface interaction are modelled, which are essential in guaranteeing suitable results that can be benchmarked effectively against experimental data. The results from this CFD simulation are critical as they inform two things: the total forces and moments that are critical in the identification of the LNMS (i.e. potential) model but also the total forces and moments that are critical for identification of the model of non-potential forces.

The model was run at a variety of depths and speeds, and the results are tabulated in Table 2. The results bear out the richness of the data, and the noteworthy changes evident in both force and moment as depth and speed change.

Initially, an attempt was made to separate the non-viscous effects from the viscous effects in the CFD simulation by removing skin friction. Since the LNMS model is a potential flow model, it was critical to isolate the potential flow effects from the simulation and express the viscous component separately. Whilst it is possible, however, to eliminate the viscous component from the flow in CFD, it is not possible to exactly extract the potential flow component. Whilst it was hoped in the beginning that the non-viscous component of the CFD simulation could serve as a reasonable surrogate for the potential component, this was found to not be the case following comparison of the ShipMo3D results with the inviscid component of the CFD output. The inviscid component of

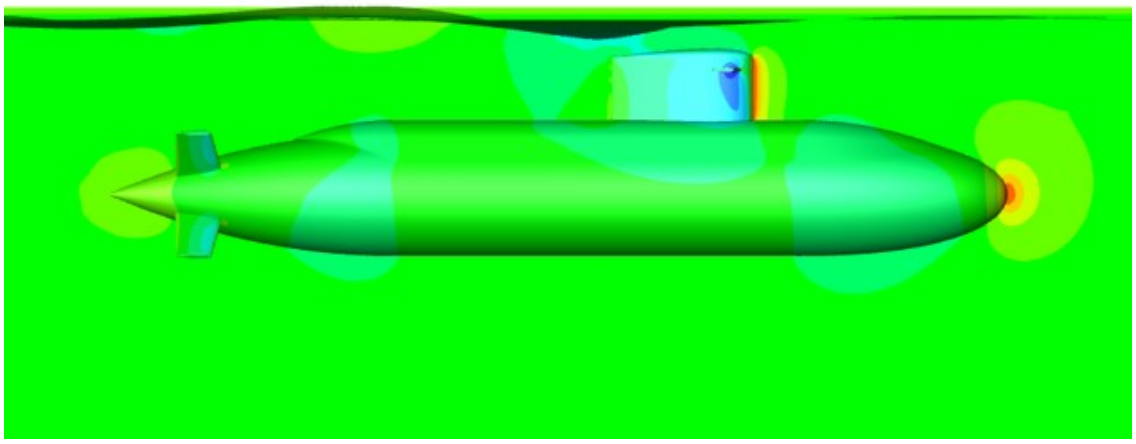

Figure 8: Flow visualisation from CFD simulation

a CFD simulation can be broken into a term due to potential flow (i.e., irrotational, inviscid flow) and another due to rotational inviscid flow. To properly identify the LNMS model, isolation of the potential component is required.

Some knowledge of the data trends across runs at different depths helped perform this isolation. For example, when collating run data as a function of depth, as deep submerged conditions are approached, it can be expected that the function representing the forces and moments will asymptote to a constant value. Application of this principle is useful, along with insight gleaned from the mathematical structure of the LNMS model, which yields trend information that can allow for correction.

The total flow model used herein is a combination of the LNMS model and a traditional depth dependent coefficient-based model used for the non-potential forces. As long as the sum of these two is correct, the model will make sound force predictions. An exception is the case where a modelling effect is exclusively represented in the LNMS model - for example wave effects. In this case, if the potential component is incorrect, a corresponding error in the force output will result.

Corroborating the LNMS wave force predictions with towing tank data ensures the split between the potential and non-potential term results in a realistic force prediction. If the non-potential model is incorrect, the total flow model will not predict the free surface suction forces in calm water sailing. If the parameters in the LNMS are incorrect, wave force predictions will be inaccurate. Towing tank data was therefore critical not just for corroboration, but also for use in the final tuning of the parameters that were identified from the CFD.